

Review

# Recent Progress on Graphene-Based Nanocomposites for Electrochemical Sodium-Ion Storage

Mai Li <sup>1,\*</sup> , Kailan Zhu <sup>1</sup>, Hanxue Zhao <sup>1</sup> and Zheyi Meng <sup>2,\*</sup><sup>1</sup> College of Science, Donghua University, Shanghai 201620, China<sup>2</sup> State Key Laboratory for Modification of Chemical Fibers and Polymer Materials, College of Materials Science, Donghua University, Shanghai 201620, China

\* Correspondence: limai@dhu.edu.cn (M.L.); mengzheyi@dhu.edu.cn (Z.M.)

**Abstract:** In advancing battery technologies, primary attention is paid to developing and optimizing low-cost electrode materials capable of fast reversible ion insertion and extraction with good cycling ability. Sodium-ion batteries stand out due to their inexpensive price and comparable operating principle to lithium-ion batteries. To achieve this target, various graphene-based nanocomposites fabricate strategies have been proposed to help realize the nanostructured electrode for high electrochemical performance sodium-ion batteries. In this review, the graphene-based nanocomposites were introduced according to the following main categories: graphene surface modification and doping, three-dimensional structured graphene, graphene coated on the surface of active materials, and the intercalation layer stacked graphene. Through one or more of the above strategies, graphene is compounded with active substances to prepare the nanocomposite electrode, which is applied as the anode or cathode to sodium-ion batteries. The recent research progress of graphene-based nanocomposites for SIBs is also summarized in this study based on the above categories, especially for nanocomposite fabricate methods, the structural characteristics of electrodes as well as the influence of graphene on the performance of the SIBs. In addition, the relevant mechanism is also within the scope of this discussion, such as synergistic effect of graphene with active substances, the insertion/deintercalation process of sodium ions in different kinds of nanocomposites, and electrochemical reaction mechanism in the energy storage. At the end of this study, a series of strategies are summarized to address the challenges of graphene-based nanocomposites and several critical research prospects of SIBs that provide insights for future investigations.

**Keywords:** graphene; nanocomposites; sodium-ion battery; electrochemical analysis; energy storage mechanism



**Citation:** Li, M.; Zhu, K.; Zhao, H.; Meng, Z. Recent Progress on Graphene-Based Nanocomposites for Electrochemical Sodium-Ion Storage. *Nanomaterials* **2022**, *12*, 2837. <https://doi.org/10.3390/nano12162837>

Academic Editors:  
Palaniappan Subramanian and  
Kalim Deshmukh

Received: 20 July 2022

Accepted: 16 August 2022

Published: 18 August 2022

**Publisher's Note:** MDPI stays neutral with regard to jurisdictional claims in published maps and institutional affiliations.



**Copyright:** © 2022 by the authors. Licensee MDPI, Basel, Switzerland. This article is an open access article distributed under the terms and conditions of the Creative Commons Attribution (CC BY) license (<https://creativecommons.org/licenses/by/4.0/>).

## 1. Introduction

Lithium-ion batteries (LIBs) are a kind of high-specific energy secondary battery that are important and widely used in commercial applications nowadays. However, due to the limitation of lithium resources, the cost of lithium-ion batteries has greatly increased recently, which will become a serious constraint for its future massive applications [1]. Therefore, sodium ion batteries (SIBs), have many advantages such as rich resources, low-cost, high-energy conversion efficiency, no over discharge characteristics, compatible with aluminum foil that make it have great application potential in new energy field [2,3]. In addition to partially replacing the highly polluting lead-acid batteries, the most significant potential application of sodium-ion batteries can also focus on balancing the peak and valley of electricity from the wind or solar power, as shown in Figure 1 [4]. People started the research on SIBs as early as the 1970s and it has witnessed a spurt of growth with the development of material science in the recent year [5]. The working principle of SIBs is similar to that of LIBs [6,7]. Its internal structure mainly contains four parts: Positive, negative, electrolyte, separator. Normally, both anode and cathode electrodes are composed

of active material powders, adhesives and conductive additives in proportion and separated using a porous separator usually made of glass fibers or porous polymers that allows ions to pass through but prevents electrons that achieve short circuit prevention [6].

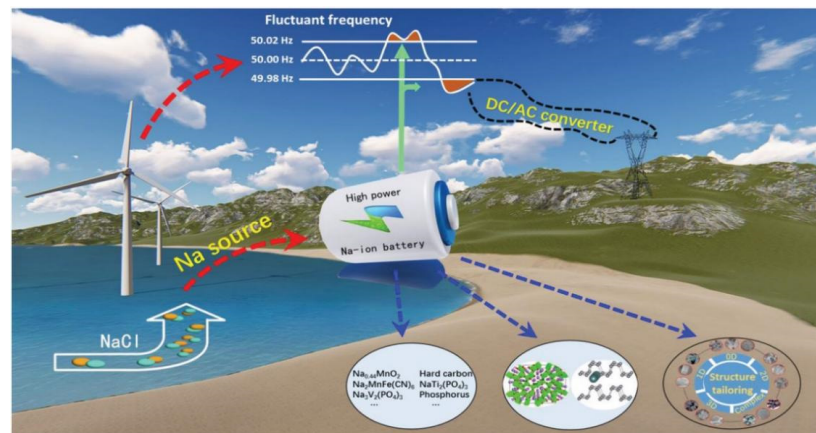


**Figure 1.** The blueprint of SIBs used in the high-power energy storage system. Reproduced with permission [4]. Copyright 2019, Wiley-VCH.

The working principle of sodium-ion battery is schematically shown in Figure 2. In essence, sodium-ion battery is an electrode with a concentration difference in ion concentration. In the process of charging the battery, the sodium ions are detached from the positive electrode, pass through the electrolyte, the separator, and transferred to the negative electrode material, the same time the electrons generated by the formation of sodium ions are passed from the outer circuit to the negative electrode, forming a closed circuit. During the discharge of the battery, the sodium ions are detached from the negative electrode and transferred to the positive through the electrolyte and separator, the electrons are also re-transferred from the negative electrode to the positive electrode of the battery through the external circuit, forming a closed loop road, to achieve charge conservation of positive and negative electrodes [8]. However, compared with lithium ion, sodium ion has a stronger solvation with the size of 1.02 Å (0.76 Å for the lithium ion) and the electrochemical potential of sodium-ion (−2.71 V, Na<sup>+</sup>/Na) is higher than that of lithium ion (−3.04 V, Li<sup>+</sup>/Li). Therefore, the electrode material of sodium-ion batteries will produce more remarkable volume changes in the charge and discharge process, resulting in more severe problems, including collapse and crushing of electrode structure. At the same time, from the perspective of dynamics, the insertion and extraction speed of larger sodium ions in electrode materials is slower than that of lithium ions, which makes sodium-ion batteries have more significant challenges in cycle life and rate capability performance [9,10].

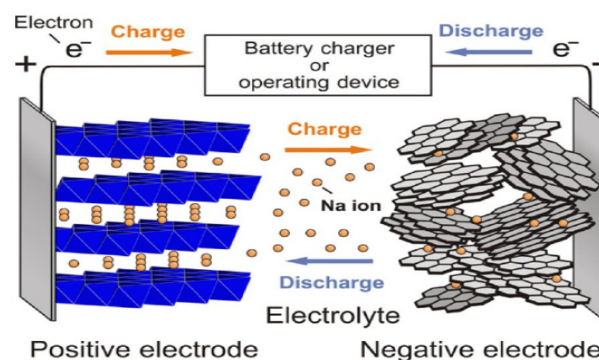


**Figure 2.** Schematic diagram of the working principle for sodium ion battery [8]. Copyright 2011, Wiley-VCH.

Up to now, to solve the above limitations, an effective method has been proved for designing nanoscale structured materials, such as nanodots [11], nanosheets [12],

nanotubes [13], nanorods [14,15], nanospheres [16], and nanocomposite structure composed of two or more of the above materials [17–19]. Considering the advantages of unique physicochemical properties, lots of exploration has triggered to realize the nanocomposites for functional energy storage applications. According to recent research, 0D nanosphere/nanoparticles, 1D nanowires/nanoneedles, 2D nanoplates/nanosheets and multi-level architectures of nanocomposite architectures have been established and shown to enhance the specific surface area, accessible pore channels, more expose active sites, and promoted ion and electron transfer [19–22]. Meanwhile, the nanocomposites have distinctive advantages such as facilitating the penetration of electrolytes, shortening the ion diffusion lengths and increasing the loading amount of active substances, resulting in improved rate ability, energy density and power density [19]. Li, M. et al., reported the nanocomposite of MnO<sub>2</sub> ultrathin nanosheet fabricated on TiN nanowires modified carbon cloth to produce the core–shell binder-free flexible electrodes for ultra-fast supercapacitor and SIBs with high voltage window. The MnO<sub>2</sub>/TiN/CC electrode showed a discharge time of 120.2 s at a current density of 2 mA cm<sup>−2</sup>, while 35 s and 34.8 s for the electrode of TiN/CC and MnO<sub>2</sub>/CC, respectively. According to the above galvanostatic charge/discharge (GCD) results, MnO<sub>2</sub>/TiN/CC electrode obtained a specific capacity of 318.41 F g<sup>−1</sup> at 2 mA cm<sup>−2</sup>, which is 2.7 times larger than that of MnO<sub>2</sub>/CC (120.5 F g<sup>−1</sup>). However, although the high porosity of the nanocomposites alleviated the volume expansion effect of materials caused by chemical reactions during the energy storage process to a certain extent, sodium ions have a larger ionic radius; this put forward a higher request for the structural stability of the composites [17,23]. Moreover, many active sodium storage materials, such as bimetallic oxides, have poor electrical conductivity [24]; organic compounds, have voltage platform and poor conductivity [25]; Prussian blue derivatives, have low coulomb efficiency and poor conductivity [26]; polyanionic compounds, have low reversible capacity ratio and some contain toxic elements [27]; which further affect the overall performance of SIBs. Therefore, nanocomposites with the advantages of avoiding the shortcomings of active materials are proposed to improve the overall electrochemical performance of SIBs. Nongkynrih J. et al., used sonochemically assisted sol gel followed by ball milling method constructed W-doped Na<sub>3</sub>V<sub>2</sub>(PO<sub>4</sub>)<sub>2</sub>F<sub>3</sub>@C as cathode material in sodium ion batteries [28]. Yi, T.F. et al., studied NiCo<sub>2</sub>S<sub>4</sub>-based nanocomposites for energy storage [29]. Sandwich architecture of graphene/MoS<sub>2</sub> composite were synthesized successfully by Yang, Z. et al., used a simple evaporation and hydrothermal reaction method as anodes for enhanced reversible lithium and sodium storage [30].

Due to the advantages such as low price, environmental friendliness, ion storability and high conductivity, carbon materials have become the optimal selection in the range of potential SIBs electrode materials [31]. Carbon materials manifest themselves as various hybridized forms of sp, sp<sup>2</sup>, and sp<sup>3</sup> that produce many allotropes with different physicochemical properties [31–34]. Graphene, the typical representative of the sp<sup>2</sup>-hybridized carbon materials composed of six-membered rings with a honeycomb structure, shows a broad application in catalysis, sensor, energy storage and other fields [35–38]. Graphene and its derivatives are widely studied. Graphene can be prepared by mechanical stripping, vapor deposition, epitaxial growth, redox and other methods [39–42]. The main preparation methods of graphene oxide include Brodie method, Staudenmaier method and Hummers method, which are all prepared by the oxidation of graphite by strong oxidizing agent in concentrated acid medium [43]. The Brodie method prepared graphene by using fuming HNO<sub>3</sub> and KClO<sub>3</sub>, the Staudenmaier method modified Brodie's method by replacing about two-thirds of the fuming HNO<sub>3</sub> with concentrated H<sub>2</sub>SO<sub>4</sub>, and the Hummers method used concentrated H<sub>2</sub>SO<sub>4</sub>, NaNO<sub>3</sub> and KMnO<sub>4</sub> to react with graphite to produce graphite oxide. The preparation methods of redox graphene mainly include chemical reduction, electrochemical reduction, thermal reduction, etc. [44–46]. Benefitting from the excellent electrical conductivity, high specific surface area, structure controllable

and good compatibility with other materials, graphene and its derived structures, such as graphene aerogel, stacked graphene layers and graphene foam have been used as the electrode for SIBs [47]. However, the pristine graphene has certain limitations in energy storage and insertion/deintercalation of sodium ions process because it does not provide sufficient active sites and the ideal amount of functional groups for enough interaction with sodium ions [31,48,49].

To solve the above problems, compatible the above-introduced nanoscale active materials with graphene is a feasible way to simultaneously stimulate the storage of energy properties of both active and carbon materials, thus ensuring fast ion/electron transfer and utilization rate of the active substance with excellent conductivity. More importantly, graphene functions as physical barrier that further buffers volume expansion and contraction of nanomaterials during the sodiation/desodiation. In addition, the synergistic effect confinements between graphene and nanoscale active materials can efficiently suppress the aggregation of both the energy storage nanomaterials and graphene during the process of material synthesis and energy storage process [18]. For instance, Ma, J.Y. et al., constructed the nanocomposite of  $\text{TiO}_2/\text{MoS}_2$  nanoflake linking with reduced graphene oxide ( $\text{TiO}_2/\text{MoS}_2/\text{RGO}$ ). Compared with  $\text{MoS}_2$  ( $200 \text{ mA h g}^{-1}$  at  $5 \text{ A g}^{-1}$ ) and  $\text{TiO}_2/\text{MoS}_2$  ( $250 \text{ mA h g}^{-1}$  at  $5 \text{ A g}^{-1}$ ), the nanocomposite showed a high specific capacity of  $310 \text{ mA h g}^{-1}$  at a current density of  $2 \text{ A g}^{-1}$  and ultrahigh structural integrity after 350 cycles [50]. The synergistic effect among RGO,  $\text{MoS}_2$  and  $\text{TiO}_2$  provides effective ion diffusion and electron transfer spaces and promotes insertion/deintercalation of Na ions that lead to the high performance of SIBs [50].

Therefore, to achieve the practical applications of sodium ion storage, various graphene-based nanocomposites fabricate stargates have been explored and can be mainly divided into the following categories according to the characteristics of the nanocomposites' structure: graphene surface modification and doping [51,52], three-dimensional structured graphene [53], graphene coated on the surface of active materials [54], the intercalation stacked two-dimensional graphene [55,56], as shown in Figure 3. Through one or more of the above strategies, graphene is compounded with active substances to prepare the nanocomposite electrode, which is applied as the anode or cathode for SIBs. In this study, the progress of graphene-based nanocomposites for SIBs is reviewed, especially for nanocomposites fabricate methods, the structural characteristics of nanocomposites as well as the influence of graphene on the performance of the SIBs based on the above categories. In addition, the relevant mechanism is also within the scope of discussion, such as the  $\text{Na}^+$  storage process in different kinds of nanocomposites, the synergistic effect of graphene and active substances, electrochemical characteristics in the energy storage process. At the end of the overview, a series of strategies are summarized to address the challenges of SIBs and several possible research directions on graphene-based nanocomposites that provide insights for future investigations.

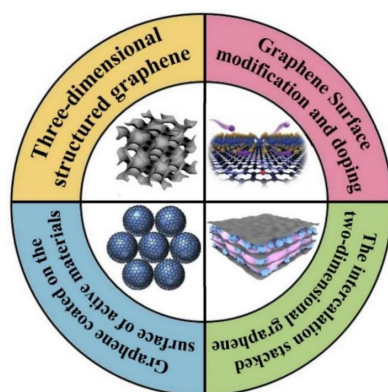


**Figure 3.** The main categories of graphene-based nanocomposites discussed in this study. Reproduced with permission [57–60]. Copyright 2018, Copyright Elsevier; 2021, Wiley-VCH; Copyright 2020, Elsevier; Copyright 2022, American Chemical Society.

## 2. Literature Review According to the Structure of Graphene-Based Nanocomposites

### 2.1. Graphene Surface Modification and Doping

The preparation of materials and structural design is fundamental aspects that should be paid attention to enhance electrochemical performance for SIBs. The active particle size, electrode porosity, conductivity and electrolyte choices together primarily determined the rate capability, energy density and cycling ability of the electrode materials [24]. Therefore, graphene as the electrically conductive and morphologically controllable functional material, which is very helpful for facilitating rapid electron and ion transportation by constructing an excellent conductive 2D layer or 3D network throughout the electrode [61]. The introduction of atoms such as N, S, P and B as active dopant sites into the graphene as the functional groups improved the chemical and electrical characteristics of the electrode and promoted practical energy storage applications [62,63]. Furthermore, the electrochemical abilities of SIBs can be further enhanced by uniformly depositing and bonding the active substance of nanoparticles on the interface or layer of graphene that modified the chemical properties of electrode. Hence, based on combining the graphene treatment methods of doping and surface modification with active materials, the conductivity accommodates the volume expansion ability, and the electrochemical performances of the nanocomposite can be enhanced through the synergistic effects [64].

Chong, S.K. et al. deposited the ultrathin MoSe<sub>2</sub> nanosheets perpendicularly onto the surface of reduced graphene oxide (MoSe<sub>2</sub>@rGO) hydrothermally as the anode for SIBs [65]. By regulating the quality ratio of graphene as 1, 5, 10, and 20% in the nanocomposite, the effects of graphene on the performance of SIBs were compared in this study. Figure 4 shows the process of preparing MoSe<sub>2</sub> and MoSe<sub>2</sub>@rGO composites by hydrothermal method with selenium powder as selenium source and sodium molybdate as molybdenum source [65]. This unique heterogeneous composite of MoSe<sub>2</sub>@rGO has a strong C–O–Mo and C–Mo interfacial bonding connection, so that the distance of crystal between MoSe<sub>2</sub> layers is expanded to 7.9 Å, which facilitates stability of structure from considerable volume changes and obtained fast electron and alkaline ion transport capability.

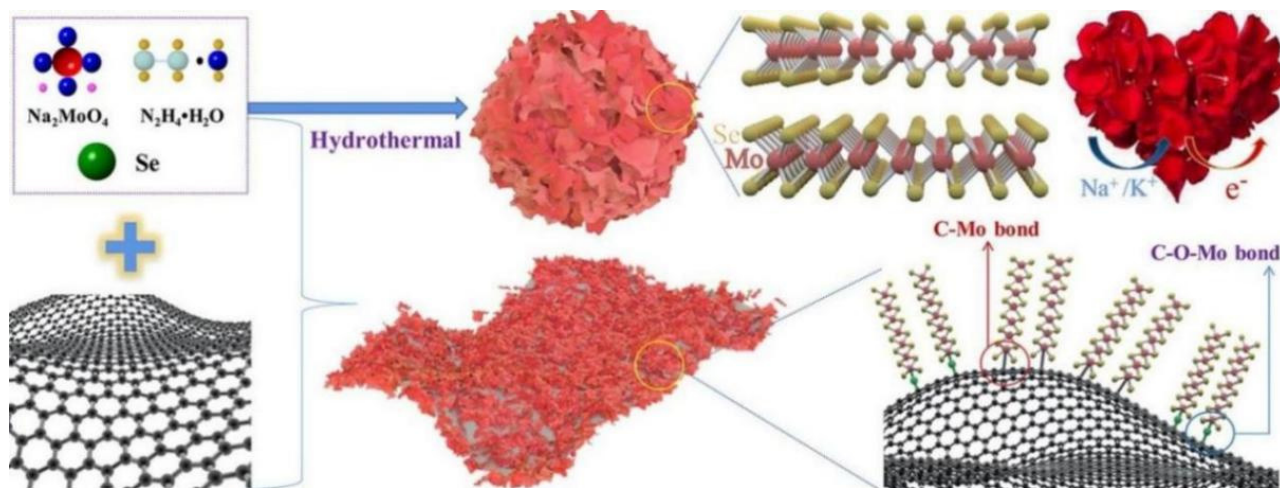


**Figure 4.** Schematic illustration of the synthetic procedure: MoSe<sub>2</sub> nanosheets perpendicularly deposition onto the surface of rGO (MoSe<sub>2</sub>@rGO). Reproduced with permission [65]. Copyright 2021, American Chemical Society.

The electrochemical performance of graphene based MoSe<sub>2</sub> SIBs were assessed from 0.01 to 3.0 V. As shown in Figure 5a, MoSe<sub>2</sub>@5%rGO as a representative for cyclic voltammetry (CV) tests to investigate the electrochemical reversibility and redox process for SIBs. During the initial CV process, five prominent peaks can be observed, among which the peaks at 1.88, 1.35, and 0.80 V corresponding to the Na<sup>+</sup> ions insertion into the layer of MoSe<sub>2</sub> to produce Na<sub>x</sub>MoSe<sub>2</sub>, which is further transformed into Mo and Na<sub>2</sub>Se [66]. The peaks at 1.07 and 0.46 V correspond to solid state interphase (SEI) film formation

and electrolyte decomposition [66]. The anodic peaks from the first to third cycle and the cathodic peaks from the second to third cycle remain at almost the same voltages, indicating excellent chemical and structural stability of the lamellar composites [66]. Figure 5b reflects the galvanostatic charge/discharge (GCD) curves of MoSe<sub>2</sub>@5% GO at 100 mA·g<sup>-1</sup> in which the plateaus match well with the CV results and the GCD curves are well overlapping after the first GCD test that manifests the reversible electrochemical properties. The first discharge/charge specific capacity of MoSe<sub>2</sub>@5%rGO can be achieved to 712.7/458.3 mAh g<sup>-1</sup> with the Coulombic efficiency of 64.3%, which is better than the specific capacity of MoSe<sub>2</sub> (622.3/338.1 mAh g<sup>-1</sup>), MoSe<sub>2</sub>@1%rGO (798.9/495.8 mAh g<sup>-1</sup>) and MoSe<sub>2</sub>@10%rGO (716.9/355.2 mAh·g<sup>-1</sup>). It also indicates that the composite materials possess highly reversible specific capacities and a good cyclic stability. Figure 5c depicts that the MoSe<sub>2</sub>@5%rGO achieved the largest retention value of 383.6 mAh·g<sup>-1</sup> after 50 cycles, which is better than the cycling stability of other rGO content. Compared with the other rGO mass content ratio in Figure 5d, under the current density of 200, 500, 1000, 2000, and 5000 mA g<sup>-1</sup>, the MoSe<sub>2</sub>@5%rGO shows the best rate capability with the capacities of 447.4, 390.0, 348.5, 306.9, and 251.3 mAh g<sup>-1</sup>, respectively. In addition, after the above GCD rate capability tests, the MoSe<sub>2</sub>@5%rGO maintained an excellent reversible capacity of 435.3 mAh g<sup>-1</sup> when the current density came back to 100 mA g<sup>-1</sup>. Therefore, MoSe<sub>2</sub>@5%rGO exhibits the optimal Na-ion storage performances by taking advantage of great kinetics and alleviating volume expansion effect from graphene and high capacity from MoSe<sub>2</sub> [65].

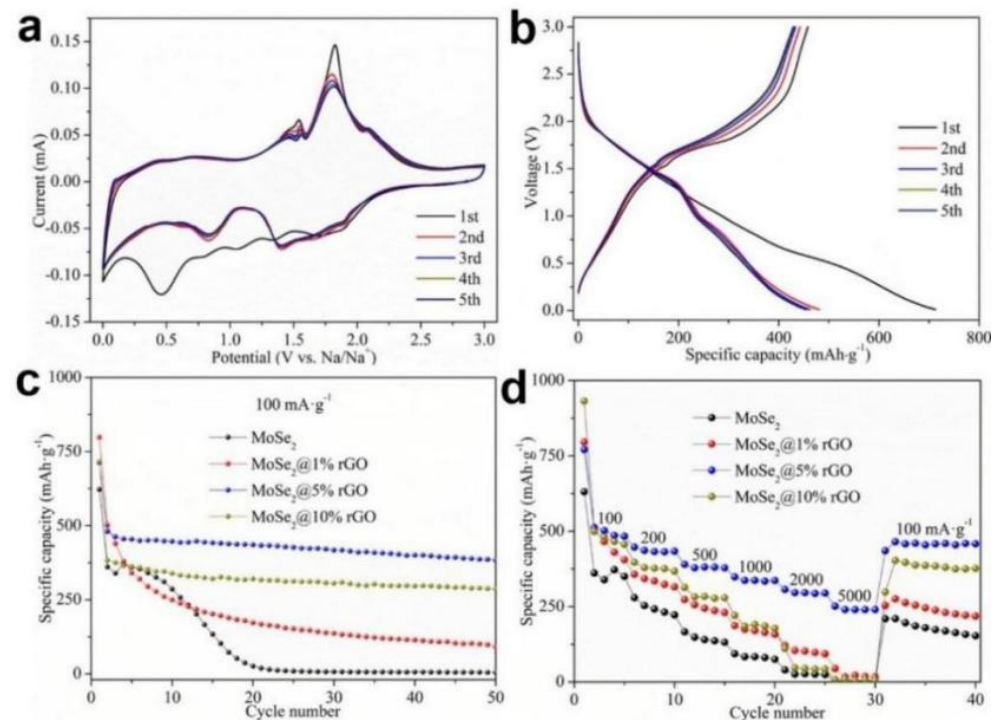


**Figure 5.** Electrochemical performance of MoSe<sub>2</sub>@rGO based SIBs: (a) CV and (b) GCD curves of MoSe<sub>2</sub>@5%rGO at 100 mA·g<sup>-1</sup>; (c) Cycling ability at the current density of 100 mA·g<sup>-1</sup>; (d) Rate capability from 100 to 5000 mA·g<sup>-1</sup>. Reproduced with permission [65]. Copyright 2020, Elsevier.

Wang, S.H. et al., fabricated the Fe<sub>2</sub>O<sub>3</sub> nanoparticles on the surface of S, N co-doped reduced graphene oxide (denoted as SNRGO) (Fe<sub>2</sub>O<sub>3</sub>/SNRGO) as the SIBs anode by microwave-assisted method [56]. The nanocomposites prepared through the microwave-assisted method have some advantages, such as low cost, Fe<sub>2</sub>O<sub>3</sub> combined closely with graphene and high preparation efficiency, which makes it possible to produce the electrode on large scale [56]. Figure 6a,b clearly show that Fe<sub>2</sub>O<sub>3</sub> nanoparticles with a diameter of around 30–80 nm is uniformly distributed on the interface of SNRGO that prevent the

agglomeration of  $\text{Fe}_2\text{O}_3$  nanoparticles and further reducing the volume change of  $\text{Fe}_2\text{O}_3$  during the  $\text{Na}^+$  insertion/extraction [67]. Consistent with SEM images, the TEM images of  $\text{Fe}_2\text{O}_3/\text{SNRGO}$  nanocomposite in Figure 6c,d confirmed that  $\text{Fe}_2\text{O}_3$  nanoparticles are deposited on the surface of SNRGO nanosheets tightly, which should be the main reason result in excellent cycle performance of SIBs.

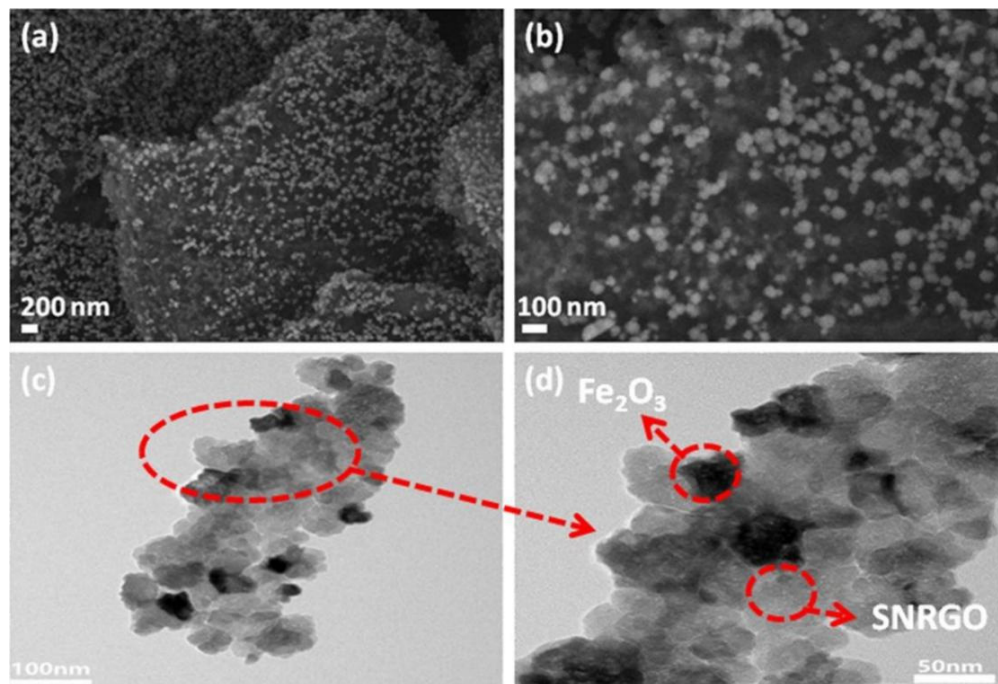


**Figure 6.** SEM images of (a) and (b)  $\text{Fe}_2\text{O}_3/\text{SNRGO}$  with different magnifications; TEM images of (c) and (d)  $\text{Fe}_2\text{O}_3/\text{SNRGO}$  with different magnifications. Reproduced with permission [56]. Copyright 2020, Elsevier.

The electrochemical behavior, including CV, GCD, rate capability performance and cycling stability of  $\text{Fe}_2\text{O}_3/\text{SNRGO}$  electrode was investigated through a half cell configuration. The CV curves of  $\text{Fe}_2\text{O}_3/\text{SNRGO}$  were carried out with a voltage window of 0.01–3 V under the scanning rate of  $0.1 \text{ mV s}^{-1}$  in the initial four cycles (Figure 7a). The two irreversible reduction peaks of 0.5 V and 1.1 V at the CV curves in the first negative scan of  $\text{Fe}_2\text{O}_3/\text{SNRGO}$  correspond to the irreversible formation of the SEI layer [68], meanwhile the reduction peak at about 0.01 V attributed to  $\text{Fe}^{3+} \rightarrow \text{Fe}^0$  [69]. In the following three CV scans, the two reduction peaks have moved to 0.63 V and 0.92 V, and in the oxidation direction, two peaks can be found at 0.66 V and 1.4 V that correspond to the reversible redox reaction of  $\text{Fe}^{3+} \leftrightarrow \text{Fe}^{2+}$  and  $\text{Fe}^{2+} \leftrightarrow \text{Fe}^0$  [70,71]. Moreover, the CV curves are well overlapping after the first CV cycle that manifests the reversible electrochemical behavior of the  $\text{Fe}_2\text{O}_3/\text{SNRGO}$  electrode. The typical GCD curves of 1st, 10th, 20th, 30th, 40th and 50th of  $\text{Fe}_2\text{O}_3/\text{SNRGO}$  based half-cell can be found in Figure 7b. In the first GCD curve, the as-prepared sample manifests a large irreversible capacity with the Coulombic efficiency of only 29.0%, which can be explained as the formation of the SEI layer due to the irreversible insertion of  $\text{Na}^+$  into the lattice [72]. It is worth noting that no obvious discharge platform has been found in the GCD curve, which is consistent with the voltage trend of the other typical  $\text{Fe}_2\text{O}_3$  based reports [67,72,73].

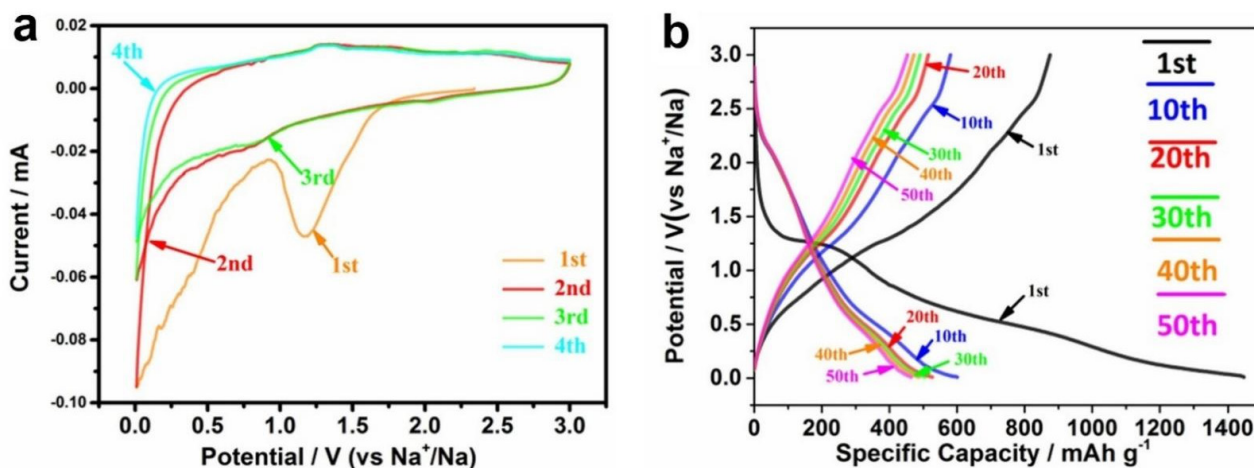


**Figure 7.** (a) CV of Fe<sub>2</sub>O<sub>3</sub>/SNRGO electrode, (b) GCD curves for the 1st, 10th, 20th, 30th, 40th and 50th cycles of Fe<sub>2</sub>O<sub>3</sub>/SNRGO electrode at 0.1 A g<sup>-1</sup>. Reproduced with permission [56]. Copyright 2020, Elsevier.

## 2.2. The Three-Dimensional Structured Graphene for SIBs

Recently, three-dimensional structured graphene as the current collector [57] compatible with the energy storage active materials [74] were used as SIBs electrode that demonstrates excellent electrochemical performance due to the synergistic effect and large surface area. The traditional process is common and uses two-dimensional materials such as copper foil and aluminum foil as the substrate, on which the active substances are coated for SIBs electrodes. Thus, in order to bind the active substances tightly on the two-dimensional foil surface, the active substance is first mixed with carbon material and binder to make slurry, and then coated on the foil [75]. Therefore, it is necessary to build a three-dimensional structure on which the active material can be firmly deposited by physical or chemical methods without the usage of binder to form the electrodes for rapid ions and electrons transportation. Due to the plasticity of graphene, the 3D structured architecture of graphene has been designed to reduce the restacking of graphene sheets during the electrode fabrication and electrochemical process and keep the large contact area with the electrolyte for enhancement of Na<sup>+</sup> storage capacity with excellent cycling stability [76]. In addition, additive-free composite not only can enhance conductivity, simplify the preparation process, reduce the cost [77], but also can meet the requirements of large specific surface area for energy storage, higher capacity, and mechanical strength [78].

Therefore, an additive-free composite of the energy storage substances with a large specific surface of three-dimensional graphene current collectors for sodium-ion storage is an ideal method to realize the next generation of high-performance SIBs with higher capacity and mechanical intensity [57].

Figure 8a depicted the fabrication procedure of hierarchical periodic thickness adjustable microlattice with micrometer pores and submillimeter filaments/channels carried out by Yan, J. et al., through a simple 3D printing method using reduced graphene oxide/carbon nanotube (rGO/CNT) aerogel [47]. As shown in Figure 8b–d, the 3D rGO/CNT microlattice aerogel has a strong electrical conductivity and abundant active nucleation sites for Na plating/stripping with a reduced current density, resulting in uniform sodium deposition to overcome the issues of dendrite. Moreover, the ion transportation rate also greatly improved due to the ordered microchannels that existed in the artificial periodic microlattice that facilitate the electrolyte permeation into the microlattice and promote the contact between active substance and electrolyte. Intrinsically, the CNTs were stable scaffolds by the rGO that improved the surface kinetics and overall conductivity synergistically, further improve the distribution of energy storage substances uniformity as well as the overall performance of the composite electrodes.

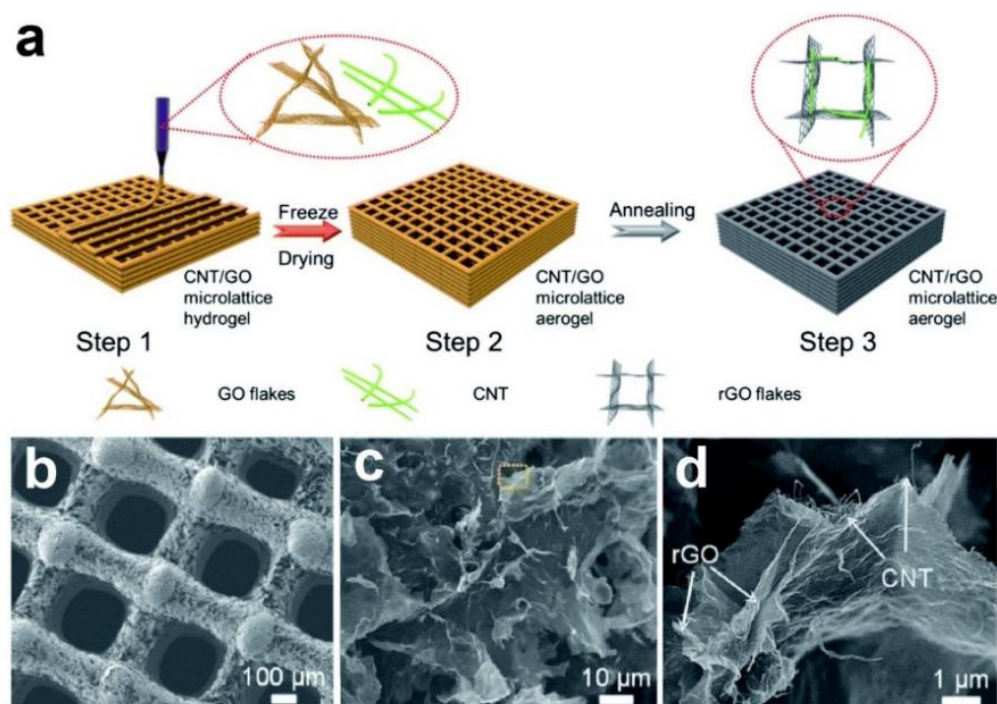


**Figure 8.** (a) The flow diagram illustrates the fabrication procedure of the printed three-dimensional rGO/CNT microlattice; (b–d) SEM images of rGO/CNT microlattice under different magnifications. Reproduced with permission [47]. Copyright 2020, Royal Society of Chemistry.

To evaluate the practical performance of rGO/CNTs microlattice aerogel for SIBs, Na metal were electrodeposition on the surface of rGO/CNT as the anode (Na@rGO/CNT) and  $\text{Na}_3\text{V}_2(\text{PO}_4)_3$  mixed with carbon on rGO (NVP@C-rGO) as the cathode were assembled into a full sodium ion battery (Figure 9a). Figure 9b depicted that under the current density of  $100 \text{ mA g}^{-1}$ , the NVP@C-rGO cathode achieved a charge/discharge capacity of  $98.8/91.1 \text{ mA h g}^{-1}$ . The performance of SIBs was also evaluated within the potential window of 2.0–3.8 V and the charge/discharge capacities of the full battery are calculated to be  $101.3 \text{ mA h g}^{-1}/93.1 \text{ mA h g}^{-1}$  at the 7th cycle (Figure 9c,d). After the active process of the first five cycles at  $20 \text{ mA g}^{-1}$ , the cycling performance was carried out at  $100 \text{ mA g}^{-1}$  and delivered good cyclic stability during 100 cycles. The long-term cycling stability of the Na@rGO/CNT//NVP@C-rGO SIBs demonstrate that the 3D printed rGO/CNT microlattice has a great potential for practical application.

Wu, D.J. et al., reported the multi-layer nanostructured graphene modified 3D macro-porous electrically conductive network (n-MECN) as the sodium ion battery substrate with superior electrochemical performance [24,79,80]. As described in the previous report and illustrated in Figure 10, the multilayer nanographene was prepared on the surface and inter-channel of MECN by solvothermal carburization method, from which the ordered porous-rich electrode substrate of n-MECN was realized [81]. In addition, then the self-branching  $\text{MnCo}_2\text{O}_4$  was hydrothermally in situ growth on the surface and inter-channel of n-MECE at  $180 \text{ }^\circ\text{C}$  to fabricate the  $\text{MnCo}_2\text{O}_4$ @n-MECN electrode. The special ordered structure with micro-channel of n-MECN not only acts as the skeleton in the electrochemical energy storage process and facilitate the transfer of electrolyte but is also compatible with the microelectronic process for the micro energy storage devices.

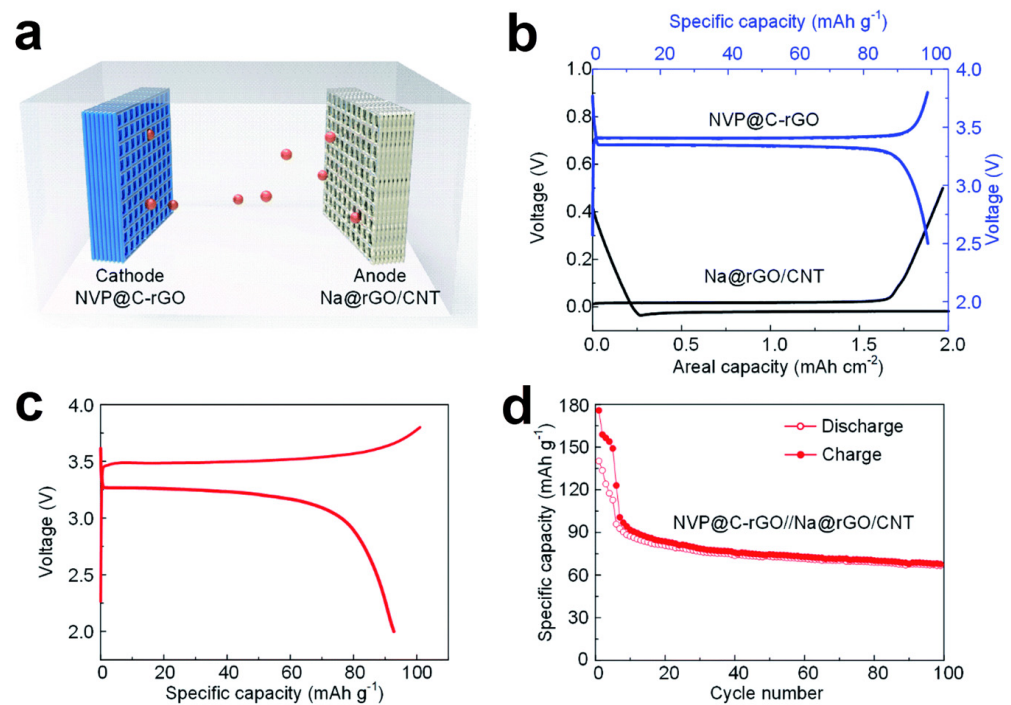


**Figure 9.** (a) Structure diagram of SIBs composite of cathode (NVP@C-rGO) and anode (Na@rGO/CNT); (b) GCD curves of the cathode (NVP@C-rGO, blue lines) and anode (Na@rGO/CNT, dark lines) half cells; (c) GCD curves of Na@rGO/CNT//NVP@C-rGO battery at 100 mA g<sup>-1</sup>; (d) The specific capacity change with the cycle number at the current density of 100 mA g<sup>-1</sup>. Reproduced with permission [47]. Copyright 2020, Royal Society of Chemistry.

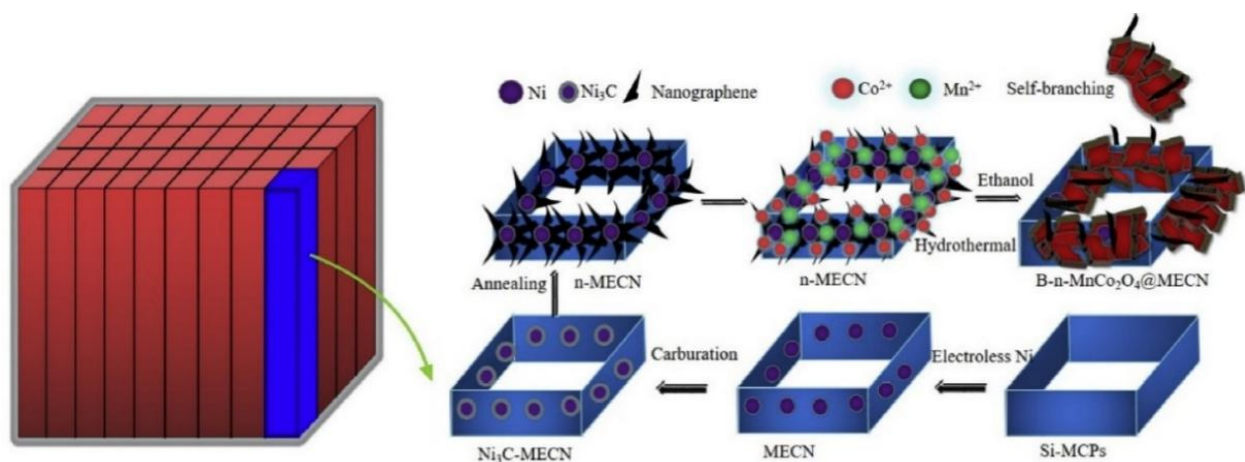


**Figure 10.** Schematic illustration of preparation steps of the MnCo<sub>2</sub>O<sub>4</sub> deposit on the nanographene modified MECN for Na-ion batteries. Reproduced with permission [79]. Copyright 2020, Elsevier.

Figure 11a,b reveal that the nanographene layers on the surface of MECN have a large number of ripples and wrinkles with a lateral size of 50–200 nm to realize the 3D electronic conductivity substrate. The 3D interconnected structure of n-MECN inherited from MECN improved the electronic conductivity and the specific surface area to facilitate electrochemical reactions. The self-branching MnCo<sub>2</sub>O<sub>4</sub> nano-architecture is incorporated into the surface (Figure 11c,d) and cross-sectional (Figure 11e,f) of n-MECN with a diameter around 50 nm, indicating that the MnCo<sub>2</sub>O<sub>4</sub>/n-MECN was successfully prepared.

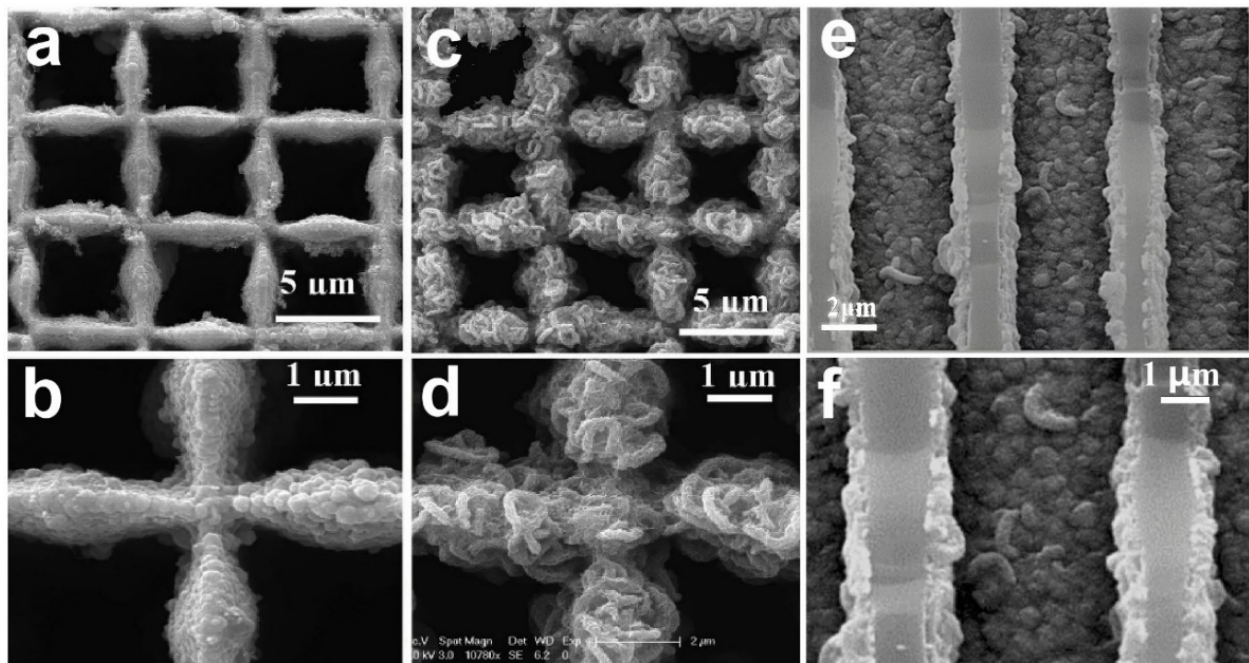


**Figure 11.** (a,b) Top view of n-MECN with different magnification; the SEM images of (c,d) Surface of  $\text{MnCo}_2\text{O}_4@n\text{-MECN}$  electrode with different magnification; (e,f) Cross-sectional images of  $\text{MnCo}_2\text{O}_4@n\text{-MECN}$  with different magnification. Reproduced with permission [79]. Copyright 2020, Elsevier.

To evaluate the practical application of the materials and structure design strategy, the  $\text{MnCo}_2\text{O}_4@n\text{-MECN}$  served as the anode in SIBs. In the cathodic process of the first CV curves cycle shown in Figure 12a, the two reduction peaks can be found at 0.25 V and 0.87 V, which are related to the irreversible formation of the SEI layer and the process of  $\text{Mn}^{2+}$  to Mn,  $\text{Co}^{3+}$  to  $\text{Co}^{2+}$ ,  $\text{Co}^{2+}$  to Co [82]. The two broad peaks related to metallic Mn to  $\text{Mn}^{2+}$  and Co to  $\text{Co}^{2+}$ ,  $\text{Co}^{2+}$  to  $\text{Co}^{3+}$  are anodic oxidation processes at 0.84 V and 1.59 V [83–85]. After the first CV cycles, the CV curves are well overlapping and the moves of the cathodic peak to 0.87 V related to the formation of the  $\text{Na}_x\text{MnCo}_2\text{O}_4$  phase, demonstrating reversible electrochemical behavior of  $\text{MnCo}_2\text{O}_4@n\text{-MECN}$  electrode [86]. Figure 12b shows the 1st, 2nd, 3rd, and 50th GCD curves of the sodium ion battery at  $50 \text{ mA g}^{-1}$ . A noticeable discharging plateau at  $\sim 0.45 \text{ V}$  can be found in the GCD curves corresponding to the reduction of  $\text{MnCo}_2\text{O}_4$  nanoarrays which is in accordance with the morphologies of CV curves [87]. The charging/discharging specific capacity calculate from the 1st GCD curve of  $\text{MnCo}_2\text{O}_4@n\text{-MECN}$  reaches  $614.7/1120.0 \text{ mAh g}^{-1}$  with the Coulombic efficiency of 75.1% [88,89]. Figure 12c reflected that  $\text{MnCo}_2\text{O}_4@n\text{-MECN}$  based SIBs show the specific capacities of 541.2, 200.5, 150.1, 110.0, and  $70.5 \text{ mAh g}^{-1}$  at the current densities of 50, 100, 200, 400, and  $800 \text{ mA g}^{-1}$ , respectively, and the reversible capacity is maintained when the current density back to  $50 \text{ mA g}^{-1}$ . As shown in Figure 12d, the SIBs reflected a good cycling ability of 100 cycles under different current densities after 1st cycle as well as the morphology and structure of  $\text{MnCo}_2\text{O}_4@n\text{-MECN}$  in SIBs are maintained after 100 cycles. Figure 12e depicted that the b value of  $\text{MnCo}_2\text{O}_4@n\text{-MECN}$  based SIBs is 0.81 at the cathodic peak indicating that the energy storage mechanism of the SIBs involves both faradic and non-faradic processes and the capacitive-controlled process makes the main contribution to the energy storage characteristics of  $\text{MnCo}_2\text{O}_4@n\text{-MECN}$ . With the increase of the scan rates the contribution of capacitive-controlled gradually increased, when scan rates from  $0.2 \text{ mv s}^{-1}$  to  $1.0 \text{ mv s}^{-1}$ , the capacitive contribution improved from 52% to 73%, and when the scanning speed is greater than  $0.8 \text{ mv s}^{-1}$ , the capacitance contribution rate hovers around 70% (Figure 12f). This study fully demonstrates that the three-dimensional structured graphene exhibits excellent electrochemical properties,

optimizing ion and electron transport, and improves the utilization of active material so as to increase the rate capability ability of the SIBs [85–87].

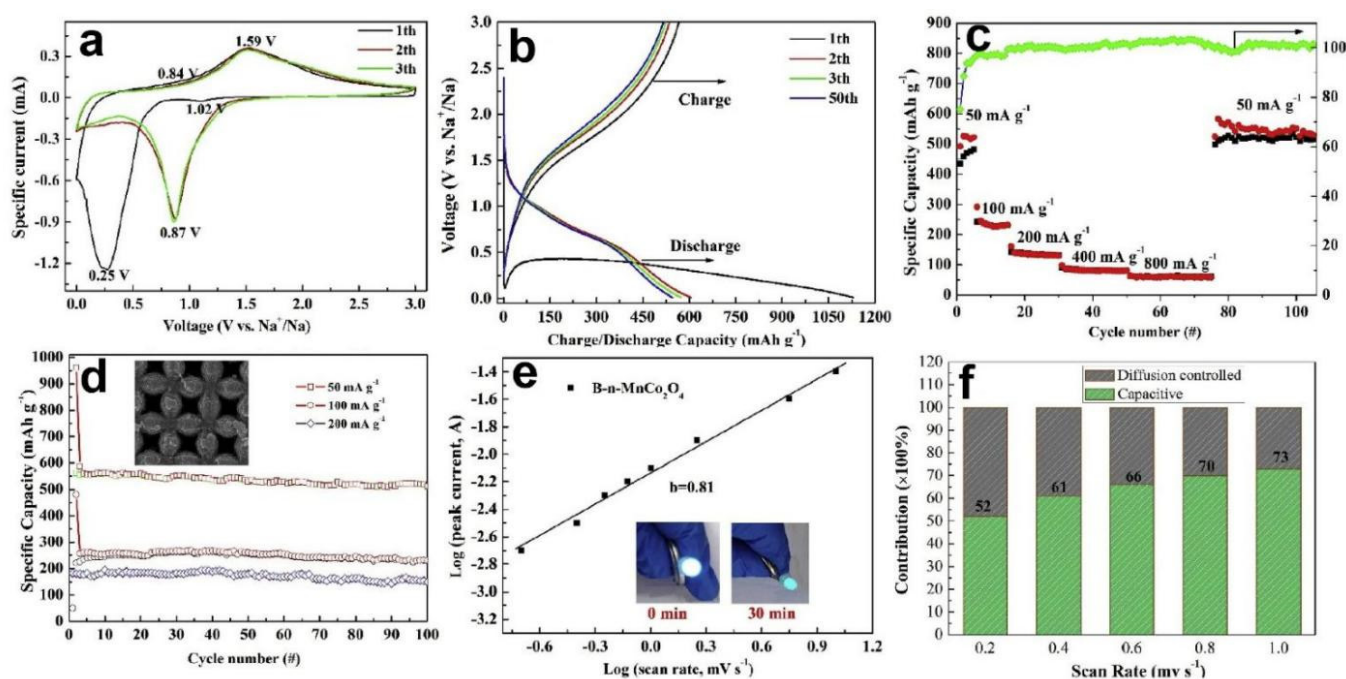


**Figure 12.** Electrochemical properties of the  $\text{MnCo}_2\text{O}_4@n\text{-MECN}$  based SIBs: (a) CV curves; (b) 1st, 2nd, 3rd, and 50th GCD curves at  $50 \text{ mA g}^{-1}$ ; (c) Rate capability performance and Coulombic efficiency from  $50 \text{ mA g}^{-1}$  to  $800 \text{ mA g}^{-1}$ ; (d) Cycling stability at  $50$ ,  $100$ , and  $200 \text{ mA g}^{-1}$ ; (e) Relationship between log scanning rates and log cathodic peak currents; (f) Normalized contribution ratio at different scan rates. Reproduced with permission [79]. Copyright 2020, Elsevier.

Jo, M.S. et al. described an electrode of graphene-based nanofibers entangled with bamboo-shaped N-CNTs containing  $\text{CoSe}_2$  nanocrystals at each node (N-CNT/rGO/ $\text{CoSe}_2$  NF) through the heat treatment process of electrospinning nanofibers [90]. Figure 13 describes the detailed formation mechanism and fabrication steps of this nanostructured electrode. An electrospinning process (Figure 13(a①)) was used to fabricate the precursor nanofibers that were composed of graphene oxide (GO), Co salt, poly (vinyl alcohol) (PVA), and PS nanobeads (40 nm). Next, the highly integrated structure of mesopores rGO nanosheets mixed with carbon-covered Co nanometals structure (Figure 13(a②)) were formed through the initial step of the first heat treatment of the precursor nanofibers with DCDA at  $400^\circ\text{C}$  under  $\text{N}_2$  atmosphere. This step initially produced Co nanometals surrounding with carbon formed by PVA decomposition that prevents the aggregation of Co nanometals. Meanwhile, during the initial step of the first heat treatment step, the uniform mesopores between the GO sheets were formed due to the decomposition of PS nanobeads distributed in the GO matrix and the GO matrix was reduced to rGO at the same time. The uniform-sized Co nanoparticles were uniformly formed in the structured mesopores when the reducing gas penetrates into the depth of the structure from the mesopores.

As shown in Figure 13(a②), the further step of the first heat treatment was carried out at  $800^\circ\text{C}$  under the  $\text{CH}_x$  and  $\text{NH}_3$  gases atmosphere and the bamboo-like N-CNTs were grown in the inner and outer parts of the rGO matrixed nanofibers by using the metallic Co nanocrystals in the mesopores as catalysts via catalytic chemical vapor deposition [91]. Interestingly, N-CNTs formed by aggregation of the C and N atoms from  $\text{CH}_x$  and  $\text{NH}_3$  gases that adsorbed and dissolved on the surface of the Co nanoparticles and the Co nanoparticles move forward by the force arising from the growth of CNTs, so that Co nanoparticles were uniformly distributed at the nodes of bamboo-like N-CNTs. Since

$\text{H}_2\text{Se}$  gas cannot penetrate the C layer of CNTs, it is difficult to convert the CNTs coated Co nanoparticles into  $\text{CoSe}_2$  directly by high temperature gas phase method, as shown in Figure 13b. Therefore, part of the CNT walls surrounding the Co nanoparticles were thermally etched during the second heat treatment step at  $300^\circ\text{C}$  for 30 min in an air atmosphere (Figure 13(a③)), although Co metal partially oxidized into  $\text{Co}_3\text{O}_4$  during this step, that was ignorable and inconsequential. Finally, in the third heat treatment step, Co and  $\text{Co}_3\text{O}_4$  nanoparticles inside the N-CNTs were selenization at  $350^\circ\text{C}$  under  $\text{H}_2\text{Se}$  gas atmosphere to form the  $\text{CoSe}_2$  nanoparticles (Figure 13(a④)). Via the above steps, the electrode of graphene-based nanofibers entangled with bamboo-shaped N-CNTs containing  $\text{CoSe}_2$  nanocrystals at each node (N-CNT/rGO/CoSe<sub>2</sub> NF) was successfully obtained. As shown in Figure 13b, selenization of Co nanocrystals captured in the walls of carbon nanotubes is very difficult because  $\text{H}_2\text{Se}$  gas used for selenization cannot penetrate the thick carbon nanotube walls. Therefore, the gas diffusion process and CO phase change can be achieved by introducing the defect part into the CNT wall during the intermediate heat treatment to achieve the goal of successfully generating  $\text{CoSe}_2$ .

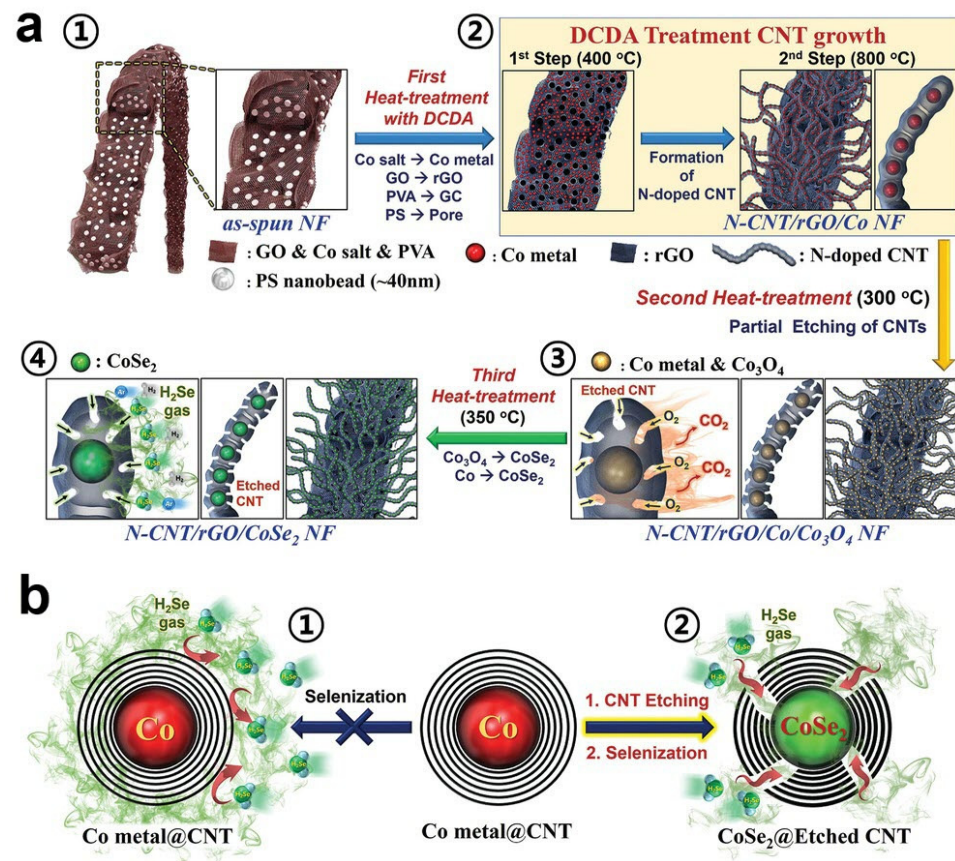


**Figure 13.** (a) Formation mechanism of the golden bristlegrass-like graphene matrixed nanofibers entangled with bamboo-like N-CNTs containing  $\text{CoSe}_2$  nanocrystals at each node and (b) efficient conversion of Co to  $\text{CoSe}_2$  by partial etching strategy of N-CNT wall. Reproduced with permission [90]. Copyright 2019, Wiley-VCH.

As shown in Figure 14a–c, the FE-SEM image of N-CNT/rGO/CoSe<sub>2</sub> NF was well-maintained throughout, even after multi-step fabrication. From the HR-TEM image of Figure 14d,e, the authors found that the diameters of the nodes in the bamboo-like N-CNTs were around 5–10 nm. The lattice spacings of 0.22 nm match well with the (111) crystal planes of  $\text{CoSe}_2$  in N-CNTs (Figure 14e) [92] and the specific peaks of the XRD pattern of N-CNT/rGO/CoSe<sub>2</sub> NF match well with the PDF#53-0449 of  $\text{CoSe}_2$  (Figure 14f) that indicating the complete selenization of Co and  $\text{Co}_3\text{O}_4$  into  $\text{CoSe}_2$  [92,93].

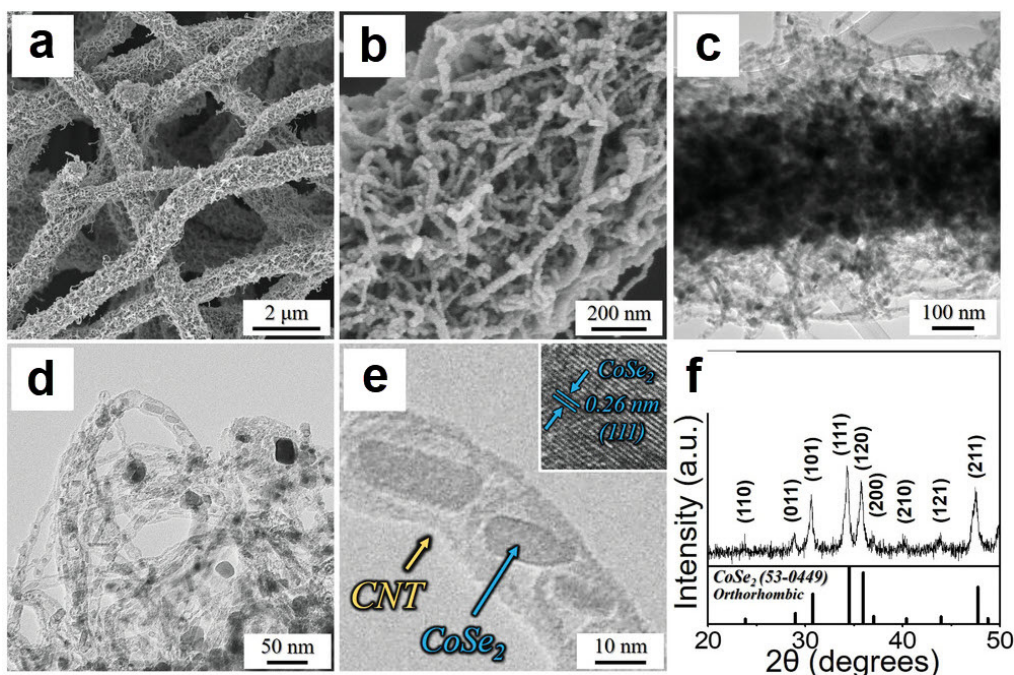


**Figure 14.** The SEM and TEM morphology and XRD characterization of N-CNT/rGO/CoSe<sub>2</sub> NF: (a,b) FE-SEM images with different magnifications, (c–e) HR-TEM images with different magnifications, (f) XRD pattern. Reproduced with permission [90]. Copyright 2019, Wiley-VCH.

In Figure 15, the electrochemical performance of the two electrodes of N-CNT/rGO/CoSe<sub>2</sub> NF and CoSe<sub>2</sub>-filled NF as the anode for SIBs were compared using carbonate-based electrolytes. At a scanning rate of 0.1 mV s<sup>-1</sup>, the initial five CV cycles of the two SIBs were carried out under the potential window of 0.001–3.0 V (Figure 14a,b). For the above two samples in the first cycle, the peak of ≈0.78 V in discharging process owing to the formation of metallic Co nanocrystals and Na<sub>2</sub>Se from the conversion reaction between the Na<sup>+</sup> and CoSe<sub>2</sub> as well as the anodic peaks at 1.84 and 1.96 V owing to the restoration of metallic Co and Na<sub>2</sub>Se into CoSe<sub>2</sub> nanocrystals in the charging process [90,92,94]. Moreover, after the first CV cycle, the insertion of Na<sup>+</sup> into CoSe<sub>2</sub> corresponded to the cathodic peaks at 1.41 and 1.11 V, and due to the formation of ultrafine CoSe<sub>2</sub> nanocrystals, the peak shift to higher potential from the second cycle [90,92,94]. Moreover, the conversion reaction with further Na<sup>+</sup> insertion was manifest at the cathodic peak of 0.7 V in the consequence CV cycles [90,94]. Figure 15c,d show the GCD curves of the N-CNT/rGO/CoSe<sub>2</sub> NF and bare CoSe<sub>2</sub>-filled NF based SIBs at a current density of 0.5 A g<sup>-1</sup> for the 1st and 2nd cycles. Typically, anode materials with crystalline materials exhibit flat plateaus and ultrafine nanocrystals or amorphous phases exhibit sloped charge/discharge profiles [95,96]. In the first discharge curve, the N-CNT/rGO/CoSe<sub>2</sub> NF manifested a comparatively short plateau at ≈0.89 V with a sloped charge/discharge profile due to the ultrafine crystallite size of the CoSe<sub>2</sub>. While the bare CoSe<sub>2</sub>-filled NF showed a lower and flatter plateau compared with CNT/rGO/CoSe<sub>2</sub> NF composite electrode due to the crystalline materials of CoSe<sub>2</sub> in CoSe<sub>2</sub>-filled NF. Bare CoSe<sub>2</sub>-filled NF shows the increase of resistance in the electrolyte due to the polarization from slow Na<sup>+</sup> ion diffusion, while the nanostructure of N-CNT/rGO/CoSe<sub>2</sub> NF has an increased Na<sup>+</sup> ion diffusion rate results a more easily Na<sup>+</sup> insertion/desertion reactions [97,98]. The initial discharge capacities of the N-CNT/rGO/CoSe<sub>2</sub> NF was 645 mA h g<sup>-1</sup> with Coulombic efficiencies of 72.4%, while the bare CoSe<sub>2</sub>-filled NF was 531 mA h g<sup>-1</sup> with the Coulombic efficiencies of 83.5%, although the active materials in N-CNT/rGO/CoSe<sub>2</sub> NF were smaller than the bare one.

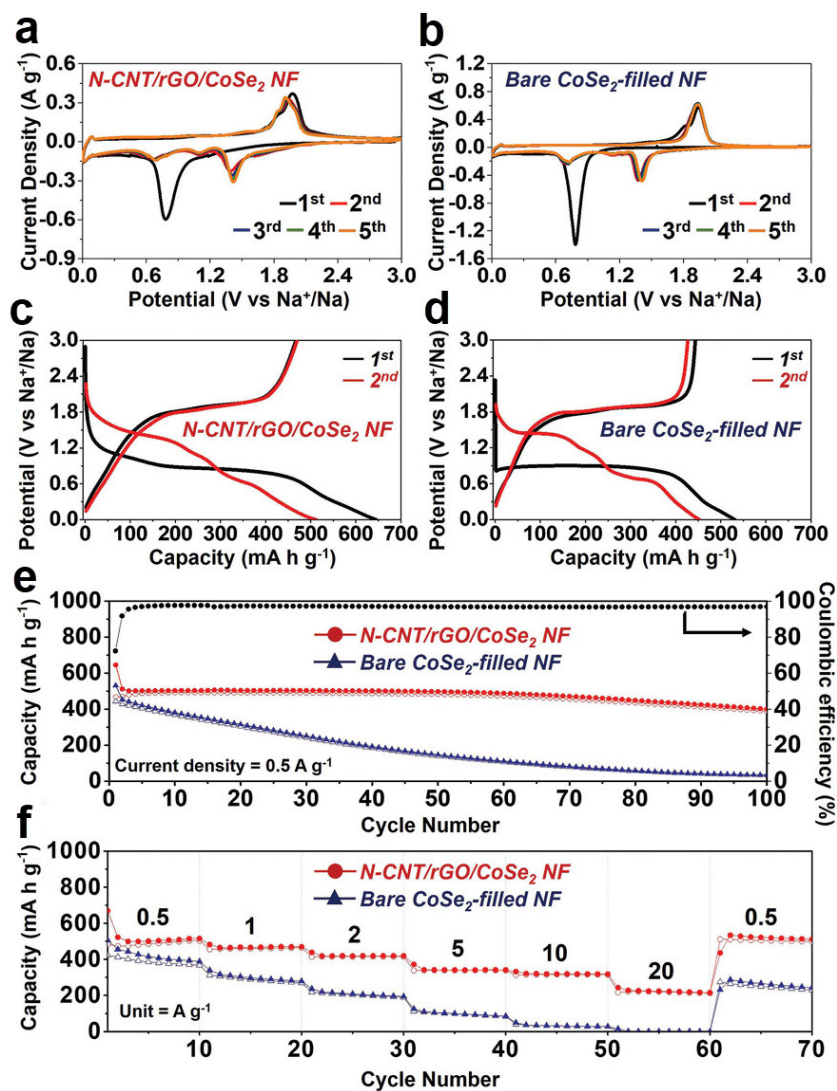


**Figure 15.** Electrochemical characteristics of N-CNT/rGO/CoSe<sub>2</sub> NF and bare CoSe<sub>2</sub>-filled NF for SIBs assembled using carbonate-based electrolytes: (a,b) CV curves, (c,d) GCD curves at 0.5 A g<sup>-1</sup>, (e) Cycle ability at 0.5 A g<sup>-1</sup>, and (f) Rate properties. Reproduced with permission [90]. Copyright 2019, Wiley-VCH.

In order to investigate the long performance of the SIBs based on N-CNT/rGO/CoSe<sub>2</sub> NF and bare CoSe<sub>2</sub>-filled NF, the cycling performance was carried out at a current density of 0.5 A g<sup>-1</sup> (Figure 15e). The bare CoSe<sub>2</sub> based SIBs exhibited a significant capacity fading that only 34 mA h g<sup>-1</sup> after the 100th cycle because of volume change and structural destruction of CoSe<sub>2</sub> during repeated insertion/extractions of Na<sup>+</sup> ion. In contrast, the N-CNT/rGO/CoSe<sub>2</sub> NF based SIBs showed the discharge capacities of 512 and 400 mA h g<sup>-1</sup> at 2nd and 100th cycles, indicating the constant cycling ability up to 100th cycles. Due to the involvement of graphene, the vertical interconnection between graphene sheets and N-CNTs embedded with CoSe<sub>2</sub> nanoparticles both restrained the aggregation and buffered the volume expansion of CoSe<sub>2</sub> nanoparticles during the cycling. To investigate the rate capacity of the nanocomposite, at current densities of 0.5, 1, 2, 5, 10, and 20 A g<sup>-1</sup>, the N-CNT/rGO/CoSe<sub>2</sub> NF achieved the discharge capacities of 516, 470, 420, 341, 318, and 215 mA h g<sup>-1</sup>, respectively (Figure 15f). Furthermore, the discharge capacity was maintained at 512 mA h g<sup>-1</sup> when the current density back to 0.5 A g<sup>-1</sup> after 60 cycles. In contrast, as the increased of current density from 0.5 to 20.0 A g<sup>-1</sup>, the discharge capacity of the bare CoSe<sub>2</sub>-filled NF decreased from 388 mA h g<sup>-1</sup> to almost zero.

### 2.3. Graphene Coated on the Surface of Active Materials

In recent years, nanomaterials uniformly encapsulated by graphene as the Na-ion battery electrodes with shortened diffusion lengths of electrons/sodium ions have been widely studied and the graphene network formed the shell enables a highly conductive matrix. The graphene shell also provides enough physical space for the volume expansion of coated nanoparticles and at the same time constrains the nanoparticles within the conductive graphene shell for stable working conditions [99]. As expected, the fabricated nanocomposites manifest outstanding electrochemical performance with both remarkable rate ability and long cycling ability. Additionally, the carbonaceous conductive graphene materials provide the pathways for electron transport that facilitate the reaction kinetics, increasing the Coulombic efficiency and stabilizing the electrode-electrolyte interfaces [58,100,101].

Tan, X.Y. et al., reported a nanocomposite based on  $\text{Sn}_4\text{P}_3$  nanoparticles coated with porous graphene tubes (GT) as the  $\text{Sn}_4\text{P}_3/\text{GT}$  for the anode of SIBs [58]. The graphene tube is composed of two layers of graphene, the inner layer is nitrogen doped hydrophilic graphene tube and the outer layer is un-doped hydrophobic graphene tubes that provide the accommodation for the volume expansion of the coated  $\text{Sn}_4\text{P}_3$  nanoparticles. N-doping not only increases the hydrophilicity contributes to the directional growth of nanomaterials and improves the electron transfer kinetic performance, but also the synergistic effect of N and graphene keeps the electrode structure stable and further improves the electrochemical performance. As illustrate in Figure 16, the graphene tubes are firstly dispersed in the aqueous solution containing tin precursor and the aqueous solution can penetrate into the hydrophilic layer of graphene tube easily. After that, the  $\text{SnO}_2$  nanoparticles prepared in the inside of the graphene tubes by selective growth of hydrothermal method and then a phosphidation process was used to forming the  $\text{Sn}_4\text{P}_3/\text{GT}$ .

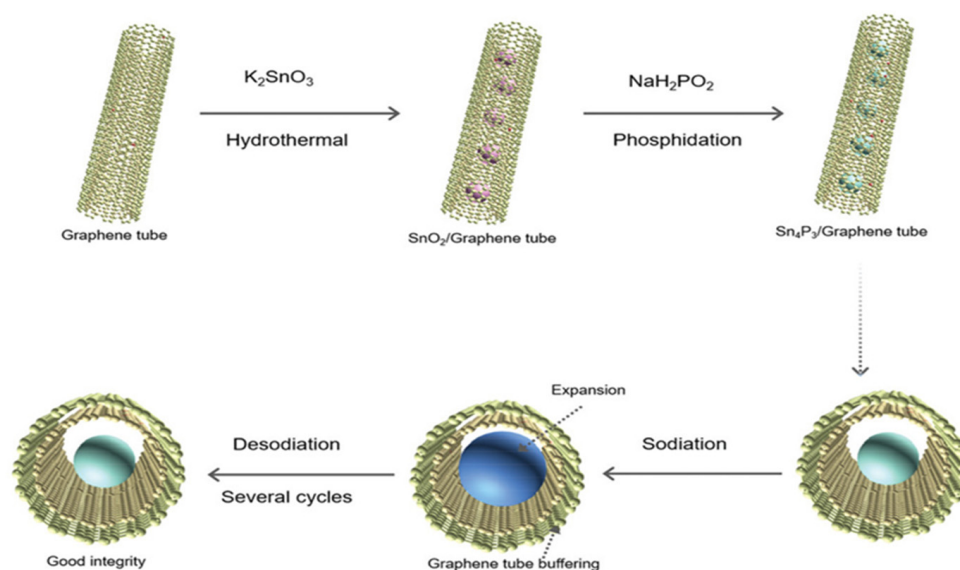


**Figure 16.** The fabrication steps the nanocomposite of  $\text{Sn}_4\text{P}_3/\text{GT}$ . The schematic illustration shows that the  $\text{SnO}_2$  nanoparticles were firstly prepared in the inside of the graphene tube by selective growth of hydrothermal method and then a phosphidation process was used to form  $\text{Sn}_4\text{P}_3/\text{GT}$ ; the following three diagrams depict the sodiation/desodiation process of  $\text{Sn}_4\text{P}_3$ . Reproduced with permission [58]. Copyright 2021, Wiley-VCH.

Figure 17a depicted that in the voltage window of 0.01–2 V (versus Na/Na<sup>+</sup>) at 0.5 A g<sup>−1</sup>, the electrode of  $\text{Sn}_4\text{P}_3/\text{GT}$  shows a first GCD curve of charge/discharge capacities of 1002 mA h g<sup>−1</sup>/722 mA h g<sup>−1</sup> with a Coulombic efficiency of 72.2%. The formation of SEI film is the main reason for the irreversible capacity during the first GCD cycle [102,103]. To realize the real application of the  $\text{Sn}_4\text{P}_3$  based nanocomposite electrode, optimization of electrolyte and further exploring SEI composition should be carried out to reduce the

initial irreversible loss for a higher Coulombic efficiency beyond 90% [104]. A capacity of  $713 \text{ mA h g}^{-1}$  has been realized after 500 cycles with well overlapping GCD curves, indicating the reversible electrochemical behavior of the  $\text{Sn}_4\text{P}_3/\text{GT}$  electrode.

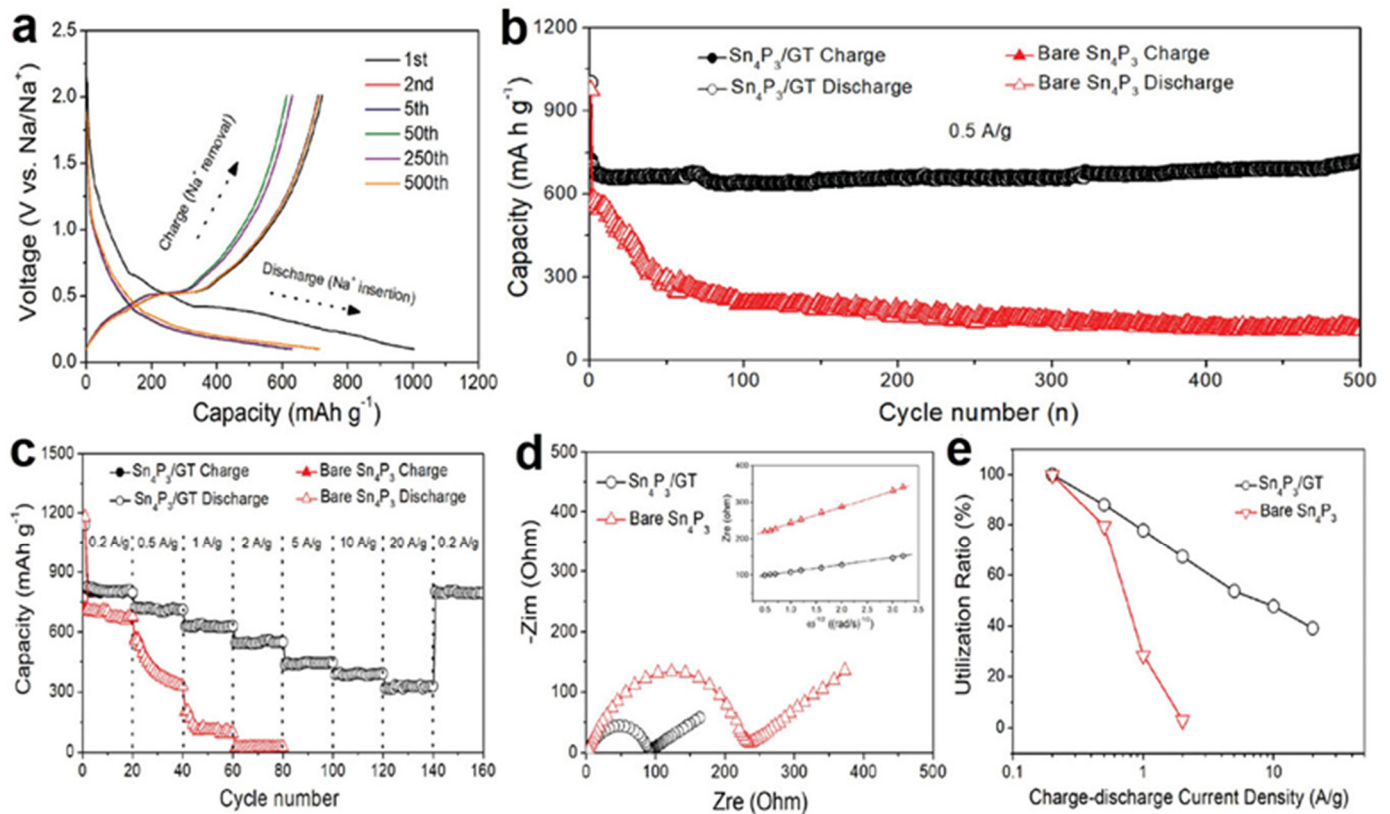


**Figure 17.** (a) GCD curves of  $\text{Sn}_4\text{P}_3/\text{GT}$  for the 1st, 2nd, 5th, 50th, 250th, and 500th cycles with the voltage window of 0.01–2 V versus  $\text{Na}/\text{Na}^+$  at  $0.5 \text{ A g}^{-1}$ ; the comparison of electrochemical properties between the electrode of  $\text{Sn}_4\text{P}_3/\text{GT}$  and bare  $\text{Sn}_4\text{P}_3$ : (b) GCD cycling tests at  $0.5 \text{ A g}^{-1}$ , (c) rate capability under different current densities for 500 cycles, (d) Nyquist plot, Inset of (d) shows the relationship between  $\omega^{-1/2}$  (where  $\omega$  is the angular frequency in the low-frequency region,  $\omega = 2\pi f$ ) and the real part of the impedance spectra ( $Z_{re}$ ), (e) Utilization ratio of the active material at different GCD current densities. Reproduced with permission [58]. Copyright 2021, Wiley-VCH.

Figure 17c depicted that the  $\text{Sn}_4\text{P}_3/\text{GT}$  electrode showed a good rate performance with the discharge capacities of 821, 722, 636, 547, 435, 386 and  $326 \text{ mA h g}^{-1}$  at current densities of 0.2, 0.5, 1, 2, 5, 10 and  $20 \text{ A g}^{-1}$ , respectively. Additionally, the discharge capacity is maintained of  $808 \text{ mA h g}^{-1}$  when the current density is back to  $0.5 \text{ A g}^{-1}$  that indicating the recoverability of the electrode. In contrast, the discharge capacity decreased from  $\sim 650 \text{ mA h g}^{-1}$  to almost zero of the bare  $\text{Sn}_4\text{P}_3$  as the current density increased from 0.2 to  $20.0 \text{ A g}^{-1}$ . The electrochemical impedance spectroscopy (EIS) was employed to further explore the performance of  $\text{Sn}_4\text{P}_3/\text{GT}$  and bare  $\text{Sn}_4\text{P}_3$  electrode with the frequency from 0.01 Hz to 10 MHz and a perturbation amplitude of 10 mV. From the Nyquist plot of Figure 17d, the  $\text{Sn}_4\text{P}_3/\text{GT}$  electrode shows a much smaller diameter of semicircle compare with bare  $\text{Sn}_4\text{P}_3$  electrode which indicate that the  $\text{Sn}_4\text{P}_3/\text{GT}$  composite electrode has a lower interfacial resistance as well as better kinetics and higher ion-diffusion rate during the process of sodiation/desodiation [105,106]. The active material utilization rate versus charge-discharge current density of the  $\text{Sn}_4\text{P}_3/\text{GT}$  and bare  $\text{Sn}_4\text{P}_3$  electrode were investigated. As shown in Figure 17e, the utilization rate of the active material in  $\text{Sn}_4\text{P}_3/\text{GT}$  decreases with the current density, which is 88%, 77%, and 67% at  $0.5 \text{ A g}^{-1}$ ,  $1 \text{ A g}^{-1}$  and  $2 \text{ A g}^{-1}$ , respectively. In contrast, the bare  $\text{Sn}_4\text{P}_3$  electrode shows the active material utilization rate of 79%, 28%, and 3% at  $0.5 \text{ A g}^{-1}$ ,  $1 \text{ A g}^{-1}$  and

$2 \text{ A g}^{-1}$ , respectively. All of the above electrochemical properties indicate that the overall performance of  $\text{Sn}_4\text{P}_3/\text{GT}$  was significantly improved by the introduction of graphene tubes on the surface of  $\text{Sn}_4\text{P}_3$  nanoparticles.

As shown in the outline in Figure 18a, the graphene-coated  $\text{Na}_{2.4}\text{Fe}_{1.8}(\text{SO}_4)_3$  (denoted as NFS) nanograins (NFS@rGO microspheres) was successfully fabricated by Fang Y.J. et al., the 3D graphene microsphere network via a spray-drying route [99]. From the SEM images of Figure 18b–d, the  $\text{Na}_{2.4}\text{Fe}_{1.8}(\text{SO}_4)_3$  nanoparticles are homogeneously distributed between layers of 3D spherical graphene and the porous in 3D graphene network are well preserved. The overall electrochemical performance of the nanocomposite of NFS@rGO was improved because of the synergistic effect between surface coated 3D graphene and  $\text{Na}_{2.4}\text{Fe}_{1.8}(\text{SO}_4)_3$  nanograins [99].

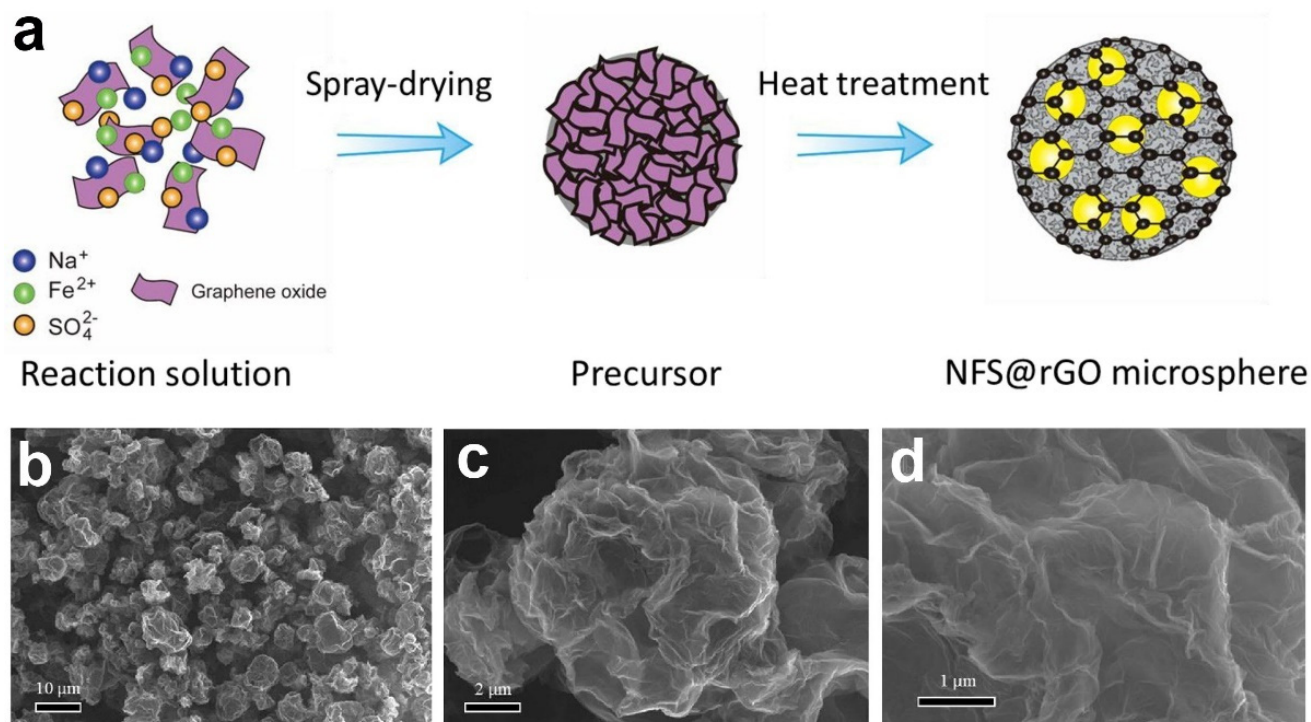


**Figure 18.** (a) The fabrication steps of NFS@rGO microspheres; (b–d) SEM images of graphene coated  $\text{Na}_{2.4}\text{Fe}_{1.8}(\text{SO}_4)_3$  microspheres with different magnifications. Reproduced with permission [99]. Copyright 2021, Elsevier.

To evaluate the sodium-storage behaviors of the materials and structure design strategy, the NFS@rGO microspheres were investigated by assembling 2016-type coin cells. As shown in Figure 19a, during the initial CV cycle, two pairs of distinct peaks can be found, while in the subsequent cycles, three pairs of peaks appeared, and the above phenomenon matches well with the previous study [107–109]. Figure 19b reflects the 1st to 4th cycles of the GCD curves of NFS@rGO microspheres at 0.05 C and the 1st charge curve shows a different shape compared to other curves, which agrees well with the CV in Figure 19a and previous research [107,108]. The reversible specific capacity of NFS@rGO electrode reaches  $100 \text{ mAh g}^{-1}$  with the average working potential of 3.75 V, obtaining an energy density of  $375 \text{ Wh kg}^{-1}$  for the corresponding full cell. Similar to CV curves, the GCD curves are almost overlapped after the initial cycle that manifests the electrode's reversible electrochemical behavior in subsequent cycles. Furthermore, it may be due to the formation of the cathode electrolyte interface layer and the irreversible decomposition of electrolyte, the Coulombic efficiency of the NFS@rGO has a certain reduction in the subsequent few cycles compared with the initial Coulombic efficiency of 89% [110].

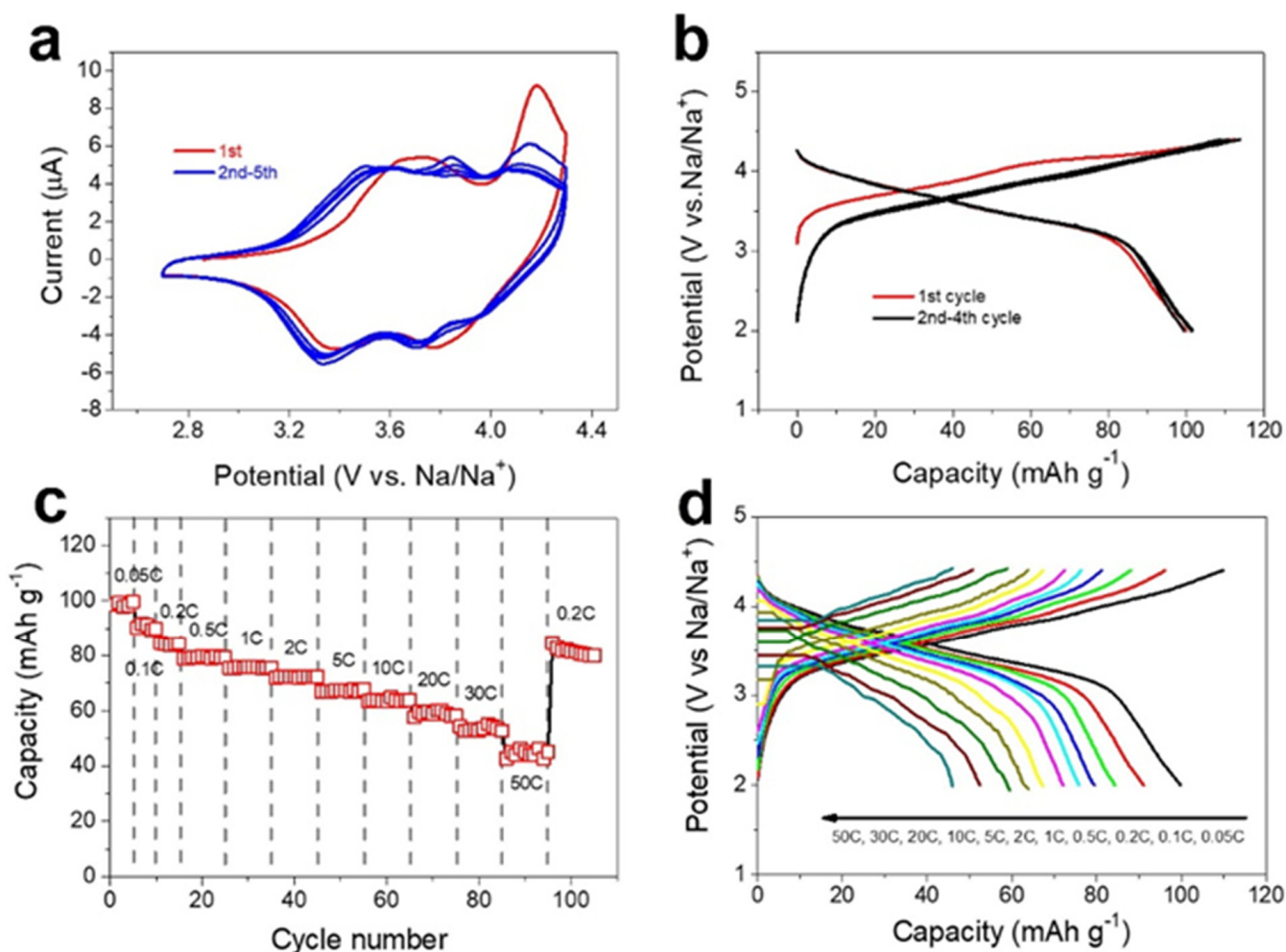


**Figure 19.** Electrochemical properties of the NFS@rGO microspheres-based electrode: (a) CV curves at a scan rate of  $0.1 \text{ mV s}^{-1}$ , (b) GCD curves performed at  $0.05 \text{ C}$  ( $1 \text{ C} = 100 \text{ mA g}^{-1}$ ), (c) Rate capacity performance, (d) GCD curves at different current density. Reproduced with permission [99]. Copyright 2021, Elsevier.

Figure 19c depicted that the SIBs full cell demonstrates a superior rate performance compared with the previous works that the reversible discharge capacities of 100, 90, 84, 80, 76, 72, 67, 64, 60, 54 and  $45 \text{ mAh g}^{-1}$  at current rate of 0.05, 0.1, 0.2, 0.5, 1, 2, 5, 10, 20, 30 and  $50 \text{ C}$ , respectively [107,111–113]. Additionally, the discharge plateaus of the NFS@rGO dropped with the increase of current rate, while the working potentials are still maintained above  $3 \text{ V}$  at a current rate even up to  $30 \text{ C}$ , better than most of the relative Fe-based cathodes, such as  $\text{FePO}_4$  [114],  $\text{NaFePO}_4$  [115],  $\text{NaFePO}_4\text{F}$  [116], and  $\text{Na}_2\text{FeP}_2\text{O}_7$  [117].

#### 2.4. Intercalation Layer Stacked Graphene

As a promising carbon material, graphene has a series of advantages, such as high conductivity, large surface area and exceptional mechanical strength [118]. Therefore, a kind of intercalation layer stacked graphene embedded in active materials between graphene layer was designed to achieve a shortened electron/ $\text{Na}^+$  transport distance with improved reaction kinetics [59]. The graphene layer act as the conducting pathway for electrons and mechanical support for nanomaterials that are confirmed to have a strong affinity to active materials, thereby mitigating the fragmentation of substances during the reaction [119]. The graphene layer and the active materials formed a sandwich electrode have a mechanically robust “nest” between the graphene layer to induce uniform deposition of active materials, therefore, inducing a strong surface capacitive contribution with high-rate capability [119]. Additionally, in the traditional electrode preparing process, polymer binders of insulation

were used to adhesion the active nanomaterials on the surface metal Cu or Al current collector, which limited the rate capability, flexibility and energy density of the active materials [3,120]. Furthermore, the interfacial bonding of the traditional electrode between active materials and metal current collectors have many limitations during the repeated sodiation/desodiation process that will cause damage to the electrode under the long-term volume expansion [118,121,122]. Therefore, constructing binder-free and freestanding electrode with layer stacked graphene sheets will obtain the mechanical flexibility, high lightweight and electrical conductivity electrodes that will effectively improve the overall performance of SIBs.

Liu, M.K. et al., designed and developed a 3D architecture by CNFs directly penetrating into graphene sheets (CNFIG) as the electrically conductive template and then the MoS<sub>2</sub> nanoflakes were in situ deposited on the surface of the CNFIG aerogel as the MoS<sub>2</sub>@CNFIG hybrid for the anode of SIBs (Figure 20a) [118]. A versatile interfacial method was first carried out to deposit the MoS<sub>2</sub> on the surface of CNFIG and then high-temperature treatment of the product of the first step to obtain the MoS<sub>2</sub>@CNFIG anode. As shown in Figure 20d–f, the layered MoS<sub>2</sub> nanoflakes were uniformly grown on both graphene layers and the CNF bridges that increasing the loading amount of the active substance. The vertically aligned channels in the inter of MoS<sub>2</sub>@CNFIG nanocomposite accelerate the penetration of electrolyte and facilitate the rapid transfer of sodium ions (Figure 20b). Since CNFIG is composed of carbon materials that provide an efficient path for rapid electron transport, facilitates the insertion/extraction ability of sodium ions.

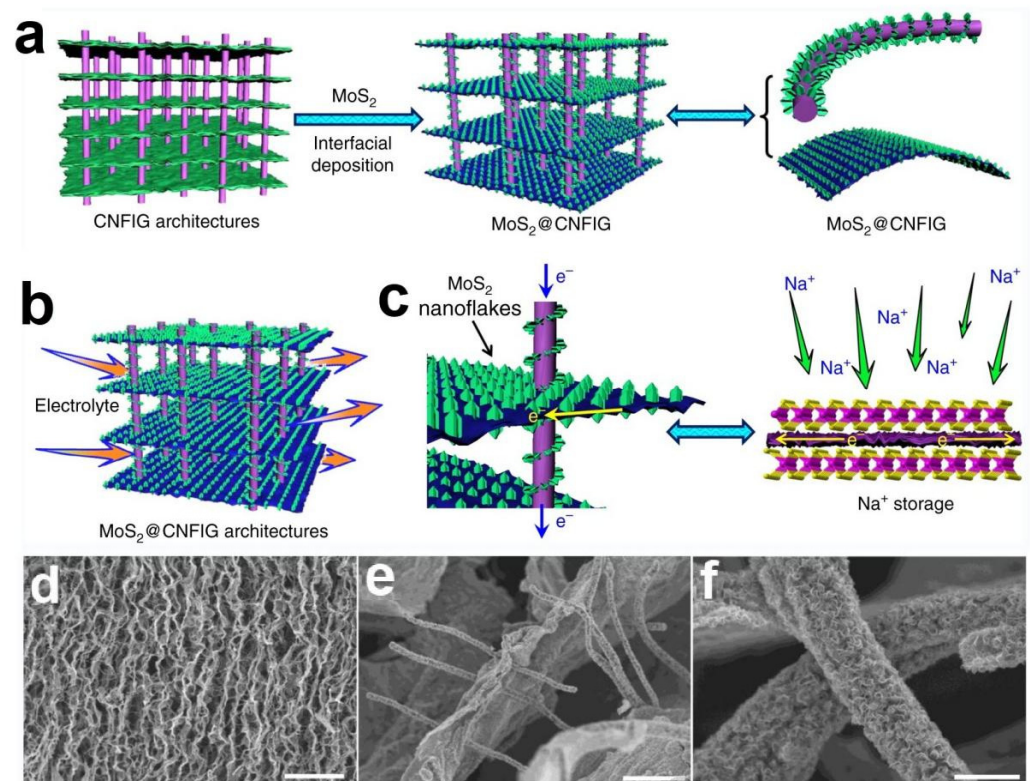


**Figure 20.** Schematic illustration of (a) homogeneous deposition of MoS<sub>2</sub> nanoflakes on layered CNFIG matrix, (b) The mechanism of porous morphology of MoS<sub>2</sub>@CNFIG nanocomposite accelerates the penetration of electrolyte and (c) the mechanism of electrically conductive MoS<sub>2</sub>@CNFIG facilitates the quick sodiation/desodiation ability and rapid transfer of sodium ions; SEM images of the MoS<sub>2</sub>@CNFIG nanocomposite: (d) overall structure with a scale bar of 50 μm and (e) cross section with scale bars of 5 μm; (f) MoS<sub>2</sub> layers uniformly deposition on the graphene layer and CNF bridges with a scale bar of 2 μm. Reproduced with permission [118]. Copyright 2019, Springer Nature.

The SEM image and corresponding EDX elemental mappings (C, Na, Mo, and S) of MoS<sub>2</sub>@CNFIG anode after 1000 cycles were applied to investigate the structural and element integrity of the MoS<sub>2</sub>@CNFIG anode. From the SEM image of Figure 21a, the porous of the MoS<sub>2</sub>@CNFIG were preserved, so that the ionic diffusion path and the volume expansion space for MoS<sub>2</sub> nanoflakes can be guaranteed during the long-time cycling. All of the above properties undoubtedly contribute to the quick sodiation/desodiation ability and rapid transfer of sodium ions. The EDX elemental mappings of C, Na, Mo, and S elements can be detected in MoS<sub>2</sub>@CNFIG anode after 1000 cycles proving that the composition of the anode was well maintained, and some sodium ions were adsorbed by the anode during the chemical redox reactions. Figure 21c shows three assembled full cells based on MoS<sub>2</sub>@CNFIG anode in parallel powering the 12 LEDs which demonstrate the potential applications of the MoS<sub>2</sub>@CNFIG nanocomposite.

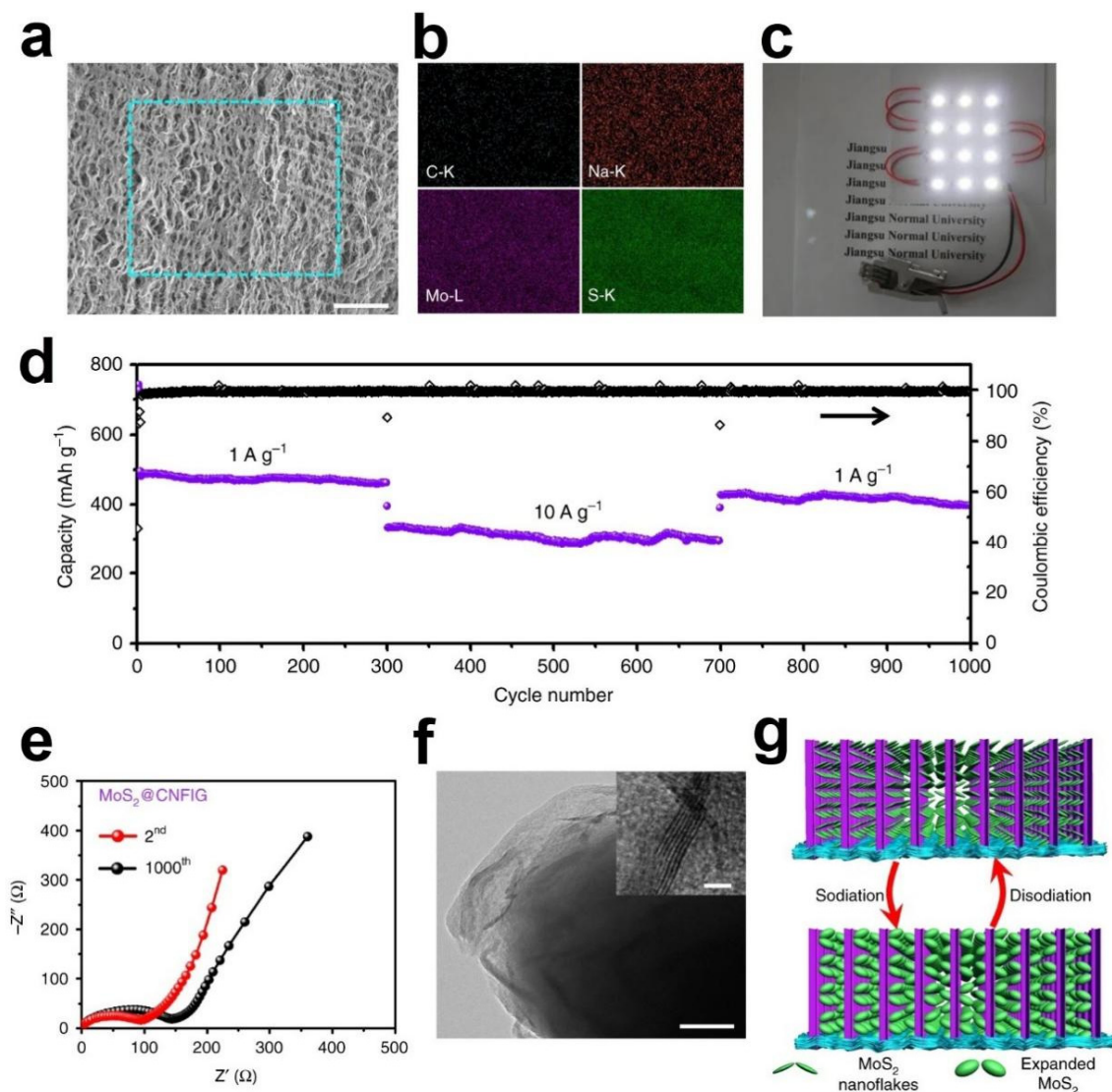


**Figure 21.** (a) SEM image (scale bar = 50  $\mu\text{m}$ ) and (b) corresponding EDX elemental mappings (C, Na, Mo, and S) of MoS<sub>2</sub>@CNFIG anode after 1000 cycles; (c) Three assembled full cells based on MoS<sub>2</sub>@CNFIG anodes in parallel powering the 12 LEDs; (d) Long-term cycling ability and Coulomb efficiency of the full cell at 1 and 10 A g<sup>-1</sup>; (e) Nyquist plots of the full cell after 2 and 1000 cycles; (f) TEM image of the full cell after 1000 cycles with the scale bar of 50 nm and 2 nm (inset in (f)); (g) Schematic illustration of porous space of CNFIG provided the volume expansion space for MoS<sub>2</sub> nanoflakes. Reproduced with permission [118]. Copyright 2019, Springer Nature.

To evaluate the rate ability and long-term cycling ability (Figure 21d), the MoS<sub>2</sub>@CNFIG anode was cycled firstly under the current density of 1 A g<sup>-1</sup> for 300 cycles and then 10 A g<sup>-1</sup> for 400 cycles with high Coulombic efficiencies approaching ~100%. The MoS<sub>2</sub>@CNFIG anode provides a capacity of 322 mA h g<sup>-1</sup> after 300 cycles at 10 A g<sup>-1</sup> and 303 mA h g<sup>-1</sup> in the 700th cycle. Additionally, the specific capacity was maintained at 421 mA h g<sup>-1</sup> when the current density back to 1 A g<sup>-1</sup> and can continue the cycle of 300 times, which indicates the recovery ability of the electrode. The excellent rate ability and cycling ability of MoS<sub>2</sub>@CNFIG nanocomposite may be ascribed to its structural stability, excellent conductive of CNFIG and the high utilization efficiency of MoS<sub>2</sub> nanoflakes with large specific surface area. The Nyquist plots of the full cell were investigated after being cycled 2 and 1000 cycles and presented in Figure 21e. The EIS spectra of the MoS<sub>2</sub>@CNFIG anode were obtained after being cycled two and 1000 times. The R<sub>ct</sub> value reflects the diameter of the semicircle in Figure 21e represents the charge-transfer resistance. The MoS<sub>2</sub>@CNFIG hybrid at 2nd cycle shows a smaller R<sub>ct</sub> value of 100 Ω compared with the R<sub>ct</sub> value of 162.3 Ω at the 1000th, indicating that the initial electrode has a lower interfacial resistance as well as better kinetics and higher ion-diffusion rate during the sodiation/desodiation process. Furthermore, the slope of the low-frequency region does not decrease much with the increase of GCD cycles, implying that the electrochemical performance of the electrode has not change significantly. From the TEM images in Figure 21f, the MoS<sub>2</sub>@CNFIG also shows clear lattice fringes with flake-like MoS<sub>2</sub> structures (inset of Figure 21f) after long-time cycles. Finally, the author attributes the excellent electrochemical storage ability of the SIBs to the 3D nested structures of MoS<sub>2</sub>@CNFIG producing nanoreservoirs between adjacent MoS<sub>2</sub> nanoflakes [121], the vertically aligned channels in CNFIG [122] and the MoS<sub>2</sub> anchored tightly on the surface of CNFIG with good electrical contact (Figure 21g).

Yang, Z.X. et al., reported the hierarchically structured graphene/MoS<sub>2</sub> composites hybrid sandwich structure (3DG-MoS<sub>2</sub>) synthesized by solution evaporation followed the hydrothermal reaction method [30]. At the synthesis stage of the sample, NH<sub>2</sub>CSNH<sub>2</sub> to the system, under hydrothermal conditions, releases H<sub>2</sub>S gas through the reaction of NH<sub>2</sub>CSNH<sub>2</sub> + 2H<sub>2</sub>O → 2NH<sub>3</sub> + H<sub>2</sub>S + CO<sub>2</sub>. After the reaction with H<sub>2</sub>S, the molybdate in G/MCu nanocomposite was converted into MoS<sub>2</sub> nanosheets [123]. In order to improve the sodium storage ability, the 3DG-MoS<sub>2</sub> nanocomposite was fabricated by embedding the Cu<sub>2</sub>O nanoparticles on the surface of graphene sheets (G/MCu) and then assembling MoS<sub>2</sub> nanosheets further on the surface of graphene sheets by hydrothermal reaction (Figure 22a) [30,124,125]. Figure 22b indicated the FE-SEM image of as-prepared G/MCu, from which we can find that the Cu<sub>2</sub>O nanoparticles have been embedded into the graphene layer with the formation of the rough surface. The cross-section FE-SEM images of G/MCu further indicated that Cu<sub>2</sub>O as the tiny particles distributed uniformly among the layers of graphene. After the hydrothermal reaction with thiourea, the molybdate in G/MCu nanocomposite was converted into MoS<sub>2</sub> nanosheets that formed the sandwich layer structure of 3DG-MoS<sub>2</sub>, as shown in Figure 22d,e. The particular architecture of layer structured graphene accelerated the penetration of electrolyte (NaClO<sub>4</sub> (1 mol/L) in DEC: EC (1:1 v/v) solution) and improved the specific surface of active material that facilitates the overall performance of SIBs.

As shown in Figure 23, the author further investigated the electrochemical performance of the 3DG-MoS<sub>2</sub> electrode under different conditions. Na storage ability of the 3DG-MoS<sub>2</sub> electrode was initially evaluated through CV curves of the 3DG-MoS<sub>2</sub> electrode at the voltage range of 0.0 to 3.0 V versus Na/Na<sup>+</sup> under the scan rate of 0.5 mVs<sup>-1</sup>. As shown in Figure 23A, a wide peak of 0.8 V can be observed in the first cycle that may be related to the insertion of sodium ions into MoS<sub>2</sub> and the irreversible formation of SEI layer [126,127]. Furthermore, the CV curves are well overlapping after the initial cycle, demonstrating excellent reversible electrochemical behavior of 3DG-MoS<sub>2</sub> electrode. Figure 23B reflects the 1st, 2nd, 5th, 10th, 50th and 100th cycles of the GCD curves of 3DG-MoS<sub>2</sub> electrode at a current density of 0.5 A g<sup>-1</sup> and the 1st charge curve shows a different shape compare with other curves, which match well with the CV in Figure 23A. The different shapes of the

first GCD curve may represent the capacity loss due to the irreversible formation of the SEI layer.

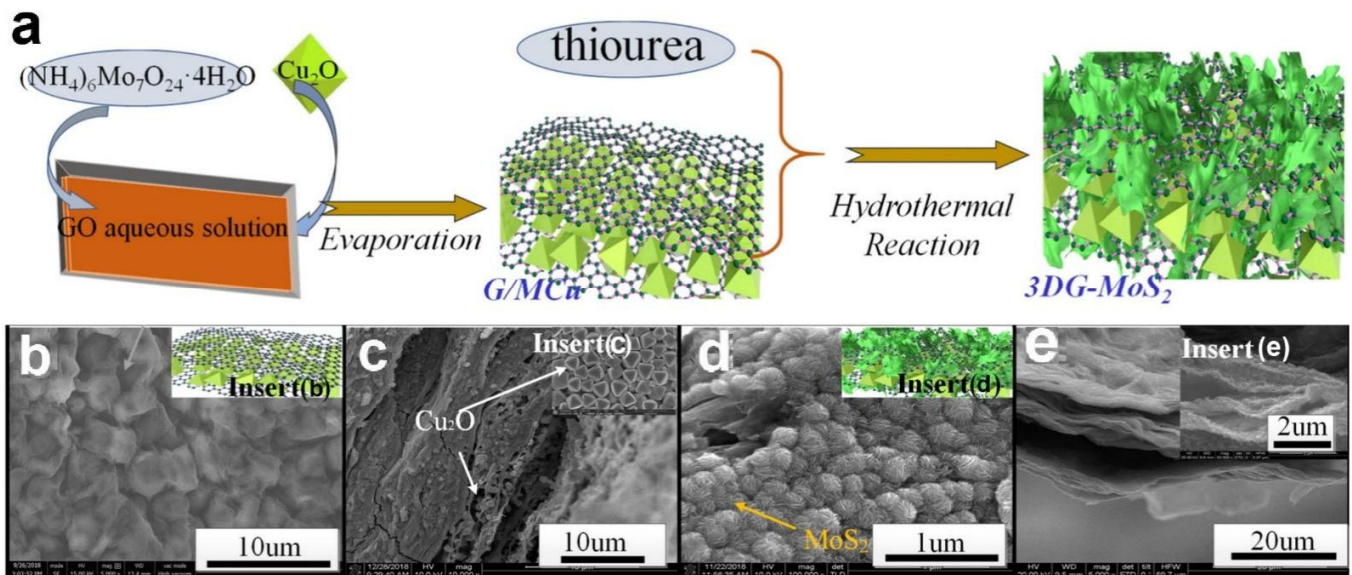


**Figure 22.** (a) Schematic illustration of the fabrication processes of 3DG-MoS<sub>2</sub>; (b) FE-SEM images of section of G/MCu and schematic structure of G/MCu (insert of (b)); (c) Cross-section FE-SEM images of G/MCu and further amplification of c (Insert of (c)); (d) FE-SEM images of 3DG-MoS<sub>2</sub> surface and schematic structure of 3DG-MoS<sub>2</sub> (Insert (d)); (e) Cross-section FE-SEM images of 3DG-MoS<sub>2</sub> with different magnifications. Reproduced with permission [30]. Copyright 2020, John Wiley and Sons.

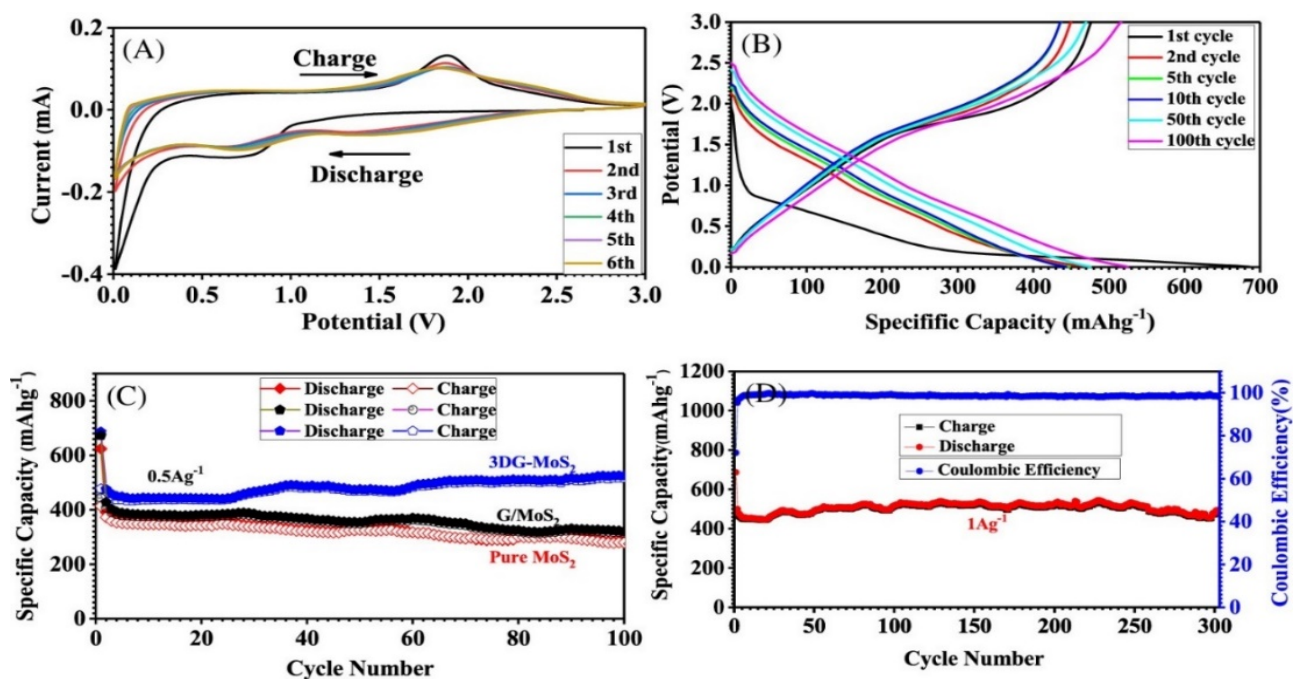


**Figure 23.** (A) CV curves of the 3DG-MoS<sub>2</sub> electrode at the voltage range of 0.0 to 3.0 V versus Na/Na<sup>+</sup> under the scan rate of 0.5 mV s<sup>-1</sup>; (B) GCD curves of the 3DG-MoS<sub>2</sub> electrode at 0.5 A g<sup>-1</sup> under different cycles; (C) Charge/discharge capacities comparison among 3DG-MoS<sub>2</sub>, MoS<sub>2</sub> nanosheets and G/MoS<sub>2</sub> at 0.5 A g<sup>-1</sup>; (D) Charge/discharge capacities and Coulomb efficiency of the 3DG-MoS<sub>2</sub> electrode at 1 A g<sup>-1</sup>. Reproduced with permission [30]. Copyright 2020, John Wiley and Sons.

To evaluate the long-term cycling ability (Figure 23C), the 3DG-MoS<sub>2</sub> electrode provides a specific capacity of 524 mAh g<sup>-1</sup> under the current density of 0.5 A g<sup>-1</sup> after 100 cycles (the slight increase of capacity with cycling may be due to activation process), which is higher than that of the G/MoS<sub>2</sub> and MoS<sub>2</sub> electrodes of 320 and 284 mAh g<sup>-1</sup>, respectively. In the author's opinion, the improvement of the cycling ability of the 3DG-MoS<sub>2</sub> electrode is mainly ascribed to the structure of the strong G/MoS<sub>2</sub> thin layers existing in 3DG/MoS<sub>2</sub> electrode, which prevents the damage caused by the volume expansion of active material. In order to further investigate the overall performance of 3DG-MoS<sub>2</sub> electrode, further 300 long-term cycling ability and Coulomb efficiency evaluations of the 3DG-MoS<sub>2</sub> electrode were carried out at a current density of 1 A g<sup>-1</sup> in Figure 23D. Obviously, the 3DG-MoS<sub>2</sub> electrode still provides a capacity up to 479 mA h g<sup>-1</sup> even after 300 cycles and exhibits the coulombic efficiency of ~100% in the whole 300 cycles except for the first one.

### 3. Discussion and Prospects

Although the graphene-based nanocomposites have been well developed in the field of new energy, there are still several key problems that should be solved to achieve high performance sodium-ion batteries for practical applications. Firstly, although a relatively comprehensive structural system of SIBs has been developed based on graphene, it is necessary to carry out the research based on more positive materials with high energy density and power density, as well as negative materials with small volume change in the process of circulation [128]. Furthermore, further improving the cycle stability of the batteries are not only an important strategy to improve the performance of sodium ion batteries, but also the critical point to realize the large-scale application of sodium ion batteries for commercial application [129]. In addition, at present, the cost of graphene-based electrodes is relatively high, and the synthesis methods of composite electrode materials are relatively complicated. More efficient strategies for combining graphene with active substances should be developed and the theoretical model of SIBs materials should be established in accordance with the development of graphene-based composite electrodes [130]. With the progress of the above technologies, sodium ion batteries can first replace the lead-acid batteries with high pollution and low energy density, and then play a greater role in more aspects. From a macro and pragmatic perspective, more research efforts of SIBs should be focused on the following four points as the prospects of this review:

(1) In-depth knowledge of Na<sup>+</sup> storage mechanism

At present, the mechanism of sodium storage is still inconclusive and needs further study, especially on low pressure platforms, ultrafine pore and closed pore filling [131]. Further studies using in/ex situ techniques [132], as well as theoretical calculations and simulations [133], are needed to better understand the role of pore size distribution, openings and closures, surface functional groups, structural defects, and pseudo graphitic domains in the sodium/desulphurization process. Developing a deeper understanding of interaction mechanism between graphene and active materials is helpful to design more novel graphene-based nanomaterials with special structures and high capacity for SIBs [134].

(2) Reasonable structure and process design of electrodes

In order to further improve the performance of the anodes, methods such as physical and chemical activation can be used. Such as: graded pore structure, microwave activation [135], H<sub>2</sub> reduction [136] and high current pretreatment [137], heteroatom doping [138], metallic NPs (or allowable materials) synthesis of nano-composite materials [139]. Some efforts should be exerted on investigating the effects of morphology, porosity, size, and defects of graphene-based electrodes to achieve better electrochemical performance [134]. Of course, in addition to some anode materials introduced in the article, it is also important to explore more efficient cathode materials and composite method of graphene based electrodes, such as Na<sub>x</sub>MO<sub>2</sub> (M = Co, Mn, Ni) [140–142], V<sub>2</sub>O<sub>5</sub> [143], V<sub>2</sub>O<sub>5</sub>·nH<sub>2</sub>O [144],

$\text{MoO}_3$  [145],  $\text{Na}_3\text{V}_2(\text{PO}_4)_3$  (NVP [146,147],  $\text{Na}_2\text{MP}_2\text{O}_7$  (M = Fe, Co, Mn) [148–150] and  $\text{NaFe}(\text{SO}_4)_2$  [151].

(3) Environmental, economic, and scaling-up aspects

By implementing low-energy processes and avoiding the use of expensive and/or hazardous chemicals, in other words, at relatively mild temperatures, SIBs can be promoted closer to commercialization by using cheaper and sustainable sources (even waste streams) such as heteroatom doping [152]. The achievement of high-quality, mass-produced, and low-cost graphene through facile methods is hard but urgent. In addition, the modification of the graphene with higher utilization efficiency should not be ignored [131]. The initial coulombic efficiency (ICE) of SIBs for both anode and cathode materials, is a key parameter for high performance SIBs, and the point is to increase the transport rate of the  $\text{Na}^+$  ions. Therefore, developing SIBs with high ICE and rate performance becomes vital to boost the commercialization of SIBs [153]. Improving initial coulombic efficiency (ICE) is due to some decomposition of electrolyte and also to the capture of irreversible sodium in pore, functional group and interlayer space. Optimizing the formulation of electrolyte and binder [141], HC engineering defects, surface area and functional groups [154], and a thorough understanding of the formation and function of SEI are essential to promoting a rational and effective electrode design [155].

(4) Full cell fabrication and commercialization of SIBs

Full-SIB devices assembled from graphene-based anodes or cathodes show promising prospects in practical applications and related performance [156–166]. Full batteries with graphene-based anodes have lower average discharge voltage when they have large capacity [156–160]. In contrast, a full battery consisting of graphene-based cathodes yields higher voltage, but its capacity and cycle capacity are unsatisfactory [165,166]. In future studies, it is worth considering the balance between voltage and capacity of all SIB based on graphene. Anodes and cathodes with high capacity, stability and suitable voltage can all achieve high performance SIBs. Further research on the application of excellent electrochemical properties in semi-batteries to full batteries and hybrid capacitors is very popular. In the case where the cathode does not provide unlimited sodium ions, it is necessary to study the anode in the full battery to evaluate its actual performance. In addition, electrolytes and additives are particularly related to the compatibility of anode and cathode materials. Building flexible SIBs is a trend of graphene-based materials [131].

#### 4. Conclusions

This review systematically introduces the combination of graphene with active substances as the nanocomposite electrodes for sodium ion electrochemical energy storage. To achieve this target, four categories of graphene-based nanocomposites fabricate stargates have been introduced in this article. Based on those categories and the research results of recent years, this review focus on the fabricate methods and structural characteristics of the graphene-based nanocomposites and the influence of graphene and morphology on the performance of the SIBs. With the development of nanotechnology as well as the excellent conductivity and plasticity of graphene, nanocomposite fabricates methods needed to be extended and expanded to stimulate the development and application of electrochemical energy storage in a benign direction. The discussion on research frontiers and applications in the field of graphene-based SIBs provide evidence that the application of graphene in advanced electrode materials is still a research hotspot, and more ingenious structure design and energy storage mechanism analysis will be the future development on the direction of nanocomposites for SIBs. Although graphene-based materials have been widely studied in SIBs and show good development prospects, their practical applications still face enormous challenges. In the first place, high-quality, large-scale production and low-cost graphene by simple methods are the basis for the production of graphene-based sodium ion batteries and should be further studied. In another, modification of graphene with higher utilization

efficiency and better understanding of the mechanism of interaction between graphene and active materials is the basis of designing new electrodes. Studying the relationship of the performance of SIBs between the morphology, porosity, size and defect of graphene-based composite electrode is the key to improve the cycle life, high Coulomb efficiency and high energy efficiency of SIBs, which is the key to the marketization of SIBs. Furthermore, reaction mechanisms and theoretical analysis associated with Na<sup>+</sup> insertion/depletion need further exploration.

**Author Contributions:** Conceptualization, M.L.; methodology, M.L.; investigation, M.L.; project administration, M.L. and Z.M.; resources, M.L. and Z.M.; supervision, M.L.; validation, M.L.; writing—original draft, M.L.; writing—review and editing, M.L., K.Z. and H.Z. All authors have read and agreed to the published version of the manuscript.

**Funding:** This research was funded by the National Natural Science Foundation of China (grant number 22005046).

**Data Availability Statement:** Not applicable.

**Conflicts of Interest:** The authors declare no conflict of interest.

## References

1. Chu, S.; Cui, Y.; Liu, N. The path towards sustainable energy. *Nat. Mater.* **2017**, *16*, 16–22. [[CrossRef](#)]
2. Yin, X.P.; Sarkar, S.; Shi, S.S.; Huang, Q.A.; Zhao, H.B.; Yan, L.M.; Zhao, Y.F.; Zhang, J.J. Recent Progress in Advanced Organic Electrode Materials for Sodium-Ion Batteries: Synthesis, Mechanisms, Challenges and Perspectives. *Adv. Funct. Mater.* **2020**, *30*, 2070071. [[CrossRef](#)]
3. Li, M.; Zhu, K.; Zhao, H.; Meng, Z.; Wang, C.; Chu, P.K. Construction of  $\alpha$ -MnO<sub>2</sub> on Carbon Fibers Modified with Carbon Nanotubes for Ultrafast Flexible Supercapacitors in Ionic Liquid Electrolytes with Wide Voltage Windows. *Nanomaterials* **2022**, *12*, 2020. [[CrossRef](#)]
4. Pu, X.; Wang, H.; Zhao, D.; Yang, H.; Ai, X.; Cao, S.; Chen, Z.; Cao, Y. Recent Progress in Rechargeable Sodium-Ion Batteries: Toward High-Power Applications. *Small* **2019**, *15*, 1805427. [[CrossRef](#)]
5. Pan, H.L.; Yong-Sheng, H.U.; Hong, L.I.; Chen, L.Q. Recent progress in structure study of electrode materials for room-temperature sodium-ion stationary batteries. *Sci. China-Chem.* **2014**, *44*, 1269.
6. Divakaran, A.M.; Minakshi, M.; Bahri, P.A.; Paul, S.; Kumari, P.; Divakaran, A.M.; Manjunatha, K.N. Rational design on materials for developing next generation lithium-ion secondary battery. *Prog. Solid State Chem.* **2021**, *62*, 100298. [[CrossRef](#)]
7. Divakaran, A.M.; Hamilton, D.; Manjunatha, K.N.; Minakshi, M. Design, development and thermal analysis of reusable Li-ion battery module for future mobile and stationary applications. *Energies* **2020**, *13*, 1477. [[CrossRef](#)]
8. Komaba, S.; Murata, W.; Ishikawa, T.; Yabuuchi, N.; Ozeki, T.; Nakayama, T.; Ogata, A.; Gotoh, K.; Fujiwara, K. Electrochemical Na insertion and solid electrolyte interphase for hard-carbon electrodes and application to Na-Ion batteries. *Adv. Funct. Mater.* **2011**, *21*, 3859–3867. [[CrossRef](#)]
9. Zhao, F.; Han, N.; Huang, W.; Li, J.; Ye, H.; Chen, F.; Li, Y. Nanostructured CuP<sub>2</sub>/C composites as high-performance anode materials for sodium ion batteries. *J. Mater. Chem. A* **2015**, *3*, 21754–21759. [[CrossRef](#)]
10. Simon, P.; Gogotsi, Y.; Dunn, B. Where Do Batteries End and Supercapacitors Begin? *Science* **2014**, *343*, 1210–1211. [[CrossRef](#)]
11. Liu, Z.; Zhang, S.; Qiu, Z.; Huangfu, C.; Wang, L.; Wei, T.; Fan, Z. Tin Nanodots derived from Sn<sup>2+</sup>/Graphene quantum dot complex as pillars into graphene blocks for ultrafast and ultrastable sodium-ion storage. *Small* **2020**, *16*, 2003557. [[CrossRef](#)]
12. Zhou, Y.; Jiang, K.; Zhao, Z.; Li, Q.; Ma, R.; Sasaki, T.; Geng, F. Giant two-dimensional titania sheets for constructing a flexible fiber sodium-ion battery with long-term cycling stability. *Energy Stor. Mater.* **2020**, *24*, 504–511. [[CrossRef](#)]
13. Liu, Y.; Zhou, B.; Liu, S.; Ma, Q.; Zhang, W.H. Galvanic Replacement Synthesis of Highly Uniform Sb Nanotubes: Reaction Mechanism and Enhanced Sodium Storage Performance. *ACS Nano* **2019**, *28*, 5885–5892. [[CrossRef](#)]
14. Cui, C.; Xu, J.; Zhang, Y.; Wei, Z.; Wang, C. Antimony Nanorod Encapsulated in Cross-Linked Carbon for High-Performance Sodium Ion Battery Anodes. *Nano Lett.* **2019**, *19*, 538–544. [[CrossRef](#)]
15. Liu, S.; Feng, J.; Bian, X.; Liu, J.; Xu, H. Advanced arrayed bismuth nanorod bundle anode for sodium-ion batteries. *J. Mater. Chem. A* **2016**, *4*, 10098–10104. [[CrossRef](#)]
16. Qiu, J.; Li, S.; Su, X.; Wang, Y.; Xu, L.; Yuan, S.; Li, H.; Zhang, S. Bismuth Nano-Spheres Encapsulated in Porous Carbon Network for Robust and Fast Sodium Storage. *Chem. Eng. J.* **2017**, *320*, 300–307. [[CrossRef](#)]
17. Li, S.; Feng, R.; Li, M.; Zhao, X.; Zhang, B.; Liang, Y.; Ning, H.; Wang, J.; Wang, C.; Chu, P.K. Needle-like CoO nanowire composites with NiO nanosheets on carbon cloth for hybrid flexible supercapacitors and overall water splitting electrodes. *RSC Adv.* **2020**, *10*, 37489–37499. [[CrossRef](#)]

18. Feng, R.; Li, M.; Wang, Y.; Lin, J.; Zhu, K.; Wang, J.; Wang, C.; Chu, P.K. High-performance multi-dimensional nitrogen-doped N+MnO<sub>2</sub>@TiC/C electrodes for supercapacitors. *Electrochim. Acta* **2021**, *370*, 137716. [[CrossRef](#)]
19. Li, M.; Zhu, K.; Meng, Z.; Hu, R.; Wang, J.; Wang, C.; Chu, P.K. Efficient coupling of MnO<sub>2</sub>/TiN on carbon cloth positive electrode and Fe<sub>2</sub>O<sub>3</sub>/TiN on carbon cloth negative electrode for flexible ultra-fast hybrid supercapacitors. *RSC Adv.* **2021**, *11*, 35726–35736. [[CrossRef](#)]
20. Pang, M.; Long, G.; Jiang, S.; Ji, Y.; Han, W.; Wang, B.; Liu, X.; Xi, Y.; Wang, D.; Xu, F. Ethanol-assisted solvothermal synthesis of porous nanostructured cobalt oxides (CoO/Co<sub>3</sub>O<sub>4</sub>) for high-performance supercapacitors. *Chem. Eng. J.* **2015**, *280*, 377–384. [[CrossRef](#)]
21. Needham, S.A.; Wang, G.X.; Liu, H.K.; Drozd, V.A.; Liu, R.S. Synthesis and electrochemical performance of doped LiCoO<sub>2</sub> materials. *J. Power Sources* **2007**, *174*, 828–831. [[CrossRef](#)]
22. Guan, C.; Wang, Y.; Hu, Y.; Liu, J.; Ho, K.H.; Zhao, W.; Fan, Z.; Shen, Z.; Zhang, H.; Wang, J. Conformally deposited NiO on a hierarchical carbon support for high-power and durable asymmetric supercapacitors. *J. Mater. Chem. A* **2015**, *3*, 23283–23288. [[CrossRef](#)]
23. Wang, J.; Zhu, G.; Zhang, Z.; Wang, Y.; Wang, H.; Bai, J.; Wang, G. Urchin-Type Architecture Assembled by Cobalt Phosphide Nanorods Encapsulated in Graphene Framework as an Advanced Anode for Alkali Metal Ion Batteries. *Chem. Eur. J.* **2021**, *27*, 1713–1723. [[CrossRef](#)]
24. Li, M.; Meng, Z.; Feng, R.; Zhu, K.; Zhao, F.; Wang, C.; Wang, J.; Wang, L.; Chu, P.K. Fabrication of Bimetallic Oxides (MCo<sub>2</sub>O<sub>4</sub>: M=Cu, Mn) on Ordered Microchannel Electro-Conductive Plate for High-Performance Hybrid Supercapacitors. *Sustainability* **2021**, *13*, 9896. [[CrossRef](#)]
25. Yan, B.; Wang, L.; Huang, W.; Zheng, S.; Hu, P.; Du, Y. High-capacity organic sodium ion batteries using a sustainable C4Q/CMK-3/SWCNT electrode. *Inorg. Chem. Front.* **2019**, *6*, 1977–1985. [[CrossRef](#)]
26. Senthilkumar, B.; Murugesan, C.; Sharma, L.; Lochab, S.; Barpanda, P. An Overview of Mixed Polyanionic Cathode Materials for Sodium-Ion Batteries. *Small Methods* **2019**, *3*, 1800253. [[CrossRef](#)]
27. Wheeler, S.; Capone, I.; Day, S.; Tang, C.; Pasta, M. Low-Potential Prussian Blue Analogues for Sodium-Ion Batteries: Manganese Hexacyanochromate. *Chem. Mater.* **2019**, *31*, 2619–2626. [[CrossRef](#)]
28. Nongkynrih, J.; Sengupta, A.; Modak, B.; Mitra, S.; Tyagi, A.K.; Dutta, P.D. Enhanced electrochemical properties of W-doped Na<sub>3</sub>V<sub>2</sub>(PO<sub>4</sub>)<sub>2</sub>F-3@C as cathode material in sodium ion batteries. *Electrochim. Acta* **2022**, *415*, 140256. [[CrossRef](#)]
29. Yi, T.-F.; Pan, J.-J.; Wei, T.-T.; Li, Y.; Cao, G. NiCo<sub>2</sub>S<sub>4</sub>-based nanocomposites for energy storage in supercapacitors and batteries. *Nano Today* **2020**, *33*, 100894. [[CrossRef](#)]
30. Yang, Z.X.; Zhang, Y.F.; Huang, J.H.; Ye, B.Q.; Lin, S.M.; Liu, J.H.; Ye, Y.L.; Zheng, K.; Lu, G.Z.; Guo, T.L.; et al. Sandwich architecture of graphene/MoS<sub>2</sub> composite as anodes for enhanced reversible lithium and sodium storage. *Int. J. Energy Res.* **2020**, *44*, 8314–8327. [[CrossRef](#)]
31. Liu, M.; Ma, Y.; Fan, X.; Singh, D.J.; Zheng, W.T. Progress of graphdiyne-based materials for anodes of alkali metal ion batteries. *Nano Futures* **2022**, *6*, 022004. [[CrossRef](#)]
32. Ivanovskii, A.L. Graphynes and graphdienes. *Prog. Solid State Chem.* **2013**, *41*, 1–19. [[CrossRef](#)]
33. Zhang, J.; Terrones, M.; Park, C.R.; Mukherjee, R.; Monthieux, M.; Koratkar, N.; Kim, Y.S.; Hurt, R.; Frackowiak, E.; Enoki, T.; et al. Carbon science in 2016: Status, challenges and perspectives. *Carbon* **2016**, *98*, 708–732. [[CrossRef](#)]
34. Xu, J.; Dou, Y.; Wei, Z.; Ma, J.; Deng, Y.; Li, Y.; Liu, H.; Dou, S. Recent Progress in Graphite Intercalation Compounds for Rechargeable Metal (Li, Na, K, Al)-Ion Batteries. *Adv. Sci.* **2017**, *4*, 1700146. [[CrossRef](#)]
35. Hernaiz, M. Applications of Graphene-Based Materials in Sensors. *Sensors* **2020**, *20*, 3196. [[CrossRef](#)]
36. Lobo, L.S.; Carabineiro, S.A.C. Kinetics of Carbon Nanotubes and Graphene Growth on Iron and Steel: Evidencing the Mechanisms of Carbon Formation. *Nanomaterials* **2021**, *11*, 143. [[CrossRef](#)]
37. Jia, Y.; Zhang, J.; Kong, D.; Zhang, C.; Han, D.; Han, J.; Tao, Y.; Lv, W.; Yang, Q.H. Practical Graphene Technologies for Electrochemical Energy Storage. *Adv. Funct. Mater.* **2022**, 2204272. [[CrossRef](#)]
38. Gunasekaran, S.S.; Kumaresan, T.K.; Masilamani, S.A.; Karazhanov, S.Z.; Raman, K.; Subashchandrabose, R. Divulging the electrochemical hydrogen storage on nitrogen doped graphene and its superior capacitive performance. *Mater. Lett.* **2020**, *273*, 127919. [[CrossRef](#)]
39. Novoselov, K.S.; Geim, A.K.; Morozov, S.V.; Jiang, D.E.; Zhang, Y.; Dubonos, S.V.; Grigorieva, I.V.; Firsov, A.A. Electric field effect in atomically thin carbon films. *Science* **2004**, *306*, 666–669. [[CrossRef](#)]
40. Stankovich, S.; Dikin, D.A.; Piner, R.D.; Kohlhaas, K.A.; Kleinhammes, A.; Jia, Y.; Wu, Y.; Nguyen, S.T.; Ruoff, R.S. Synthesis of graphene-based nanosheets via chemical reduction of exfoliated graphite oxide. *Carbon* **2007**, *45*, 1558–1565. [[CrossRef](#)]
41. Reina, A.; Jia, X.; Ho, J.; Nezich, D.; Son, H.; Bulovic, V.; Dresselhaus, M.S.; Kong, J. Large area, few-layer graphene films on arbitrary substrates by chemical vapor deposition. *Nano Lett.* **2009**, *9*, 30–35. [[CrossRef](#)] [[PubMed](#)]
42. Berger, C.; Song, Z.; Li, T.; Li, X.; Ogbazghi, A.Y.; Feng, R.; Dai, Z.; Marchenkov, A.N.; Conrad, E.H.; First, P.N.; et al. Ultrathin epitaxial graphite: 2D electron gas properties and a route toward graphene-based nanoelectronics. *J. Phys. Chem. B* **2004**, *108*, 19912–19916. [[CrossRef](#)]
43. Hummers Jr, W.S.; Offeman, R.E. Preparation of graphitic oxide. *J. Am. Chem. Soc.* **1958**, *80*, 1339. [[CrossRef](#)]

44. Li, D.; Müller, M.B.; Gilje, S.; Kaner, R.B.; Wallace, G.G. Processable aqueous dispersions of graphene nanosheets. *Nat. Nanotechnol.* **2008**, *3*, 101–105. [[CrossRef](#)]
45. Toh, S.Y.; Loh, K.S.; Kamarudin, S.K.; Daud, W.R.W. The impact of electrochemical reduction potentials on the electrocatalytic activity of graphene oxide toward the oxygen reduction reaction in an alkaline medium. *Electrochim. Acta* **2016**, *199*, 194–203. [[CrossRef](#)]
46. McAllister, M.J.; Li, J.L.; Adamson, D.H.; Schniepp, H.C.; Abdala, A.A.; Liu, J.; Herrera-Alonso, M.; Milius, D.L.; Car, R.; Prud'homme, R.K.; et al. Single sheet functionalized graphene by oxidation and thermal expansion of graphite. *Chem. Mater.* **2007**, *19*, 4396–4404. [[CrossRef](#)]
47. Yan, J.; Zhi, G.; Kong, D.Z.; Wang, H.; Xu, T.T.; Zang, J.H.; Shen, W.X.; Xu, J.M.; Shi, Y.M.; Dai, S.G.; et al. 3D printed rGO/CNT microlattice aerogel for a dendrite-free sodium metal anode. *J. Mater. Chem. A* **2020**, *8*, 19843–19854. [[CrossRef](#)]
48. Yao, F.; Li, B.; So, K.; Chang, J.; Ly, T.H.; Vu, A.Q.; Mun, H.; Cojocar, C.S.; Yue, H.; Xie, S. A strategy to overcome the limits of carbon-based materials as lithium-ion battery anodes. *Carbon* **2014**, *79*, 563–571. [[CrossRef](#)]
49. Guo, H.; Long, D.; Zheng, Z.; Chen, X.; Ng, A.; Lu, M. Defect-enhanced performance of a 3D graphene anode in a lithium-ion battery. *Nanotechnology* **2017**, *28*, 505402. [[CrossRef](#)]
50. Ma, J.; Xing, M.; Yin, L.; Hui, K.S.; Hui, K.N. Porous hierarchical TiO<sub>2</sub>/MoS<sub>2</sub>/RGO nanoflowers as anode material for sodium ion batteries with high capacity and stability. *Appl. Surf. Sci.* **2021**, *536*, 147735. [[CrossRef](#)]
51. Jaoude, M.A.; Alhseinat, E.; Polychronopoulou, K.; Bharath, G.; Banat, F. Morphology-dependent electrochemical performance of MnO<sub>2</sub> nanostructures on graphene towards efficient capacitive deionization. *Electrochim. Acta* **2019**, *330*, 135202. [[CrossRef](#)]
52. Wang, S.; Zhu, Y.; Sun, X.; Liu, H.; Cui, J.; Zhang, Y.; He, W. N, S co-doped modified graphene/Fe<sub>2</sub>O<sub>3</sub> composites synthesized via microwave-assisted method for Na-ion batteries. *Inorg. Chem. Commun.* **2020**, *121*, 108188. [[CrossRef](#)]
53. Li, H.; Wang, X.; Zhao, Z.; Tian, Z.; Zhang, D.; Wu, Y. Ni<sub>2</sub>P Nanoflake Array/Three-Dimensional Graphene Architecture as Integrated Free-Standing Anode for Boosting the Sodiation Capability and Stability. *ChemElectroChem* **2018**, *6*, 404–412. [[CrossRef](#)]
54. Tan, X.; Mo, R.; Xu, J.; Li, X.; Yin, Q.; Shen, L.; Lu, Y. High Performance Sodium Ion Anodes Based on Sn<sub>4</sub>P<sub>3</sub> Encapsulated within Amphiphilic Graphene Tubes. *Adv. Energy Mater.* **2022**, *12*, 2102345. [[CrossRef](#)]
55. Yong, L.; Dy, C.; Ys, B.; Yong, W.B.; Bs, D.; Wen, L.B.; Rui, G.B.; Hp, B.; Hz, C.; Jz, C. Recycling materials from degraded lithium-ion batteries for Na-ion storage. *Mater. Today Energy* **2020**, *15*, 100368.
56. Dong, O.; JI, C.; Mjla, B.; Ju, Y.; Jo, A.; Shk, A.; Kmk, A.; Ygl, A. Restacked nanohybrid graphene layers with expanded interlayer distance enabled by inorganic spacer for highly efficient, flexible Na-ion battery anodes—Science Direct. *J. Electroanal. Chem.* **2021**, *886*, 115137.
57. Han, J.; Liu, P.; Ito, Y.; Guo, X.; Hirata, A.; Fujita, T.; Chen, M. Bilayered nanoporous graphene/molybdenum oxide for high-rate lithium ion batteries. *Nano Energy* **2018**, *45*, 273–279. [[CrossRef](#)]
58. Zhang, X.; Weng, W.; Gu, H.; Hong, Z.; Xiao, W.; Wang, F.; Li, W.; Gu, D. Versatile Preparation of Mesoporous Single-Layered Transition-Metal Sulfide/Carbon Composites for Enhanced Sodium Storage. *Adv. Mater.* **2022**, *34*, 2104427. [[CrossRef](#)]
59. Thangavel, R.; Kannan, A.G.; Ponraj, R.; Yoon, G.; Aravindan, V.; Kim, D.W.; Kang, K.; Yoon, W.S.; Lee, Y.S. Surface enriched graphene hollow spheres towards building ultra-high power sodium-ion capacitor with long durability. *Energy Storage Mater.* **2020**, *25*, 702–713. [[CrossRef](#)]
60. He, Q.; Jin, X.; Li, Z.; Cai, Z.; Tian, J.; Hui, J.; Zhang, H. Regulated Electrodeposition of Na Metal in Monolithic ZIF-Pillared Graphene Anodes. *ACS Appl. Mater. Interfaces* **2022**, *14*, 1203–1211. [[CrossRef](#)]
61. Ma, M.; Yao, Y.; Wu, Y.; Yu, Y. Progress and Prospects of Transition Metal Sulfides for Sodium Storage. *Adv. Fiber Mater.* **2020**, *2*, 314–337. [[CrossRef](#)]
62. Ai, W.; Luo, Z.; Jiang, J.; Zhu, J.; Du, Z.; Fan, Z.; Xie, L.; Zhang, H.; Huang, W.; Yu, T. Nitrogen and sulfur codoped graphene: Multifunctional electrode materials for high-performance Li-Ion batteries and oxygen reduction reaction. *Adv. Mater.* **2014**, *26*, 6186–6192. [[CrossRef](#)] [[PubMed](#)]
63. Li, W.; Zhou, M.; Li, H.; Wang, K.; Cheng, S.; Jiang, K. A high performance sulfur-doped disordered carbon anode for sodium ion batteries. *Energy Environ. Sci.* **2015**, *8*, 2916–2921. [[CrossRef](#)]
64. Harids, A.K.; Sadan, M.K.; Kim, H.H.; Heo, J.; Kim, S.S.; Choi, C.H.C.; Jung, H.Y.; Ahn, H.J.; Ahn, J.H. Realizing high-performance Li/Na-Ion half/full batteries via the synergistic coupling of Nano-Iron sulfide and S-doped graphene. *ChemSusChem* **2021**, *14*, 1936–1947. [[CrossRef](#)]
65. Chong, S.; Wei, X.; Wu, Y.; Sun, L.; Huang, W. Expanded MoSe<sub>2</sub> Nanosheets Vertically Bonded on Reduced Graphene Oxide for Sodium and Potassium-Ion Storage. *ACS Appl. Mater. Inter.* **2021**, *13*, 13158–13169. [[CrossRef](#)]
66. Zhao, X.; Sui, J.; Li, F.; Fang, H.; Wang, H.; Li, J.; Cai, W.; Cao, G. Lamellar MoSe<sub>2</sub> nanosheets embedded with MoO<sub>2</sub> nanoparticles: Novel hybrid nanostructures promoted excellent performances for lithium ion batteries. *Nanoscale* **2016**, *8*, 17902–17910. [[CrossRef](#)]
67. Meng, S.; Zhao, D.-L.; Wu, L.-L.; Ding, Z.-W.; Cheng, X.W.; Hu, T. Fe<sub>2</sub>O<sub>3</sub>/nitrogen-doped graphene nanosheet nanocomposites as anode materials for sodium-ion batteries with enhanced electrochemical performance. *J. Alloys Compd.* **2018**, *737*, 130–135. [[CrossRef](#)]

68. Li, T.; Qin, A.; Yang, L.; Chen, J.; Wang, Q.; Zhang, D.; Yang, H. In situ grown Fe<sub>2</sub>O<sub>3</sub> single crystallites on reduced graphene oxide nanosheets as high performance conversion anode for Sodium-Ion batteries. *ACS Appl. Mater. Inter.* **2017**, *9*, 19900–19907. [[CrossRef](#)]
69. Shi, L.; Li, Y.; Zeng, F.; Ran, S.; Dong, C.; Leu, S.-Y.; Boles, S.T.; Lam, K.H. In situ growth of amorphous Fe<sub>2</sub>O<sub>3</sub> on 3D interconnected nitrogen-doped carbon nanofibers as high-performance anode materials for sodium-ion batteries. *Chem. Eng. J.* **2019**, *356*, 107–116. [[CrossRef](#)]
70. Saraf, M.; Natarajan, K.; Mobin, S.M. Microwave assisted fabrication of a nanostructured reduced graphene oxide (rGO)/Fe<sub>2</sub>O<sub>3</sub> composite as a promising next generation energy storage material. *RSC Adv.* **2017**, *7*, 309–317. [[CrossRef](#)]
71. Kong, D.; Cheng, C.; Wang, Y.; Liu, B.; Huang, Z.; Yang, H.Y. Seed-assisted growth of  $\alpha$ -Fe<sub>2</sub>O<sub>3</sub> nanorod arrays on reduced graphene oxide: A superior anode for high-performance Li-ion and Na-ion batteries. *J. Mater. Chem. A* **2016**, *4*, 11800–11811. [[CrossRef](#)]
72. Wang, S.; Wang, W.; Zhan, P.; Jiao, S. Hollow  $\alpha$ -Fe<sub>2</sub>O<sub>3</sub> Nanospheres Synthesized Using a Carbon Template as Novel Anode Materials for Na-Ion Batteries. *ChemElectroChem* **2014**, *1*, 1636–1639. [[CrossRef](#)]
73. Jian, Z.; Zhao, B.; Liu, P.; Li, F.; Zheng, M.; Chen, M.; Shi, Y.; Zhou, H. Fe<sub>2</sub>O<sub>3</sub> nanocrystals anchored onto graphene nanosheets as the anode material for low-cost sodium-ion batteries. *Chem. Commun.* **2014**, *50*, 1215–1217. [[CrossRef](#)] [[PubMed](#)]
74. Dong, C.; Guo, L.; He, Y.; Chen, C.; Qian, Y.; Chen, Y.; Xu, L. Sandwich-like Ni<sub>2</sub>P nanoarray/nitrogen-doped graphene nanoarchitecture as a high-performance anode for sodium and lithium-ion batteries. *Energy Storage. Mater.* **2018**, *15*, 234–241. [[CrossRef](#)]
75. Guo, H.; Chen, C.; Chen, K.; Cai, H.; Chang, X.; Liu, S.; Li, W.; Wang, Y.; Wang, C. High performance carbon coated hollow Ni<sub>12</sub>P<sub>5</sub> nanocrystals decorated on GNS as advanced anodes for lithium and sodium storage. *J. Mater. Chem. A* **2017**, *5*, 22316–22324. [[CrossRef](#)]
76. Ma, X.; Ji, C.; Liu, Y.; Yu, X.; Xiong, X. Oxygen-rich graphene vertically grown on 3D N-Doped carbon foam for high-performance sodium ion batteries. *J. Power Sources* **2022**, *530*, 231292. [[CrossRef](#)]
77. Chen, W.; Deng, D. Carbonized common filter paper decorated with Sn@C nanospheres as additive-free electrodes for sodium-ion batteries. *Carbon* **2015**, *87*, 70–77. [[CrossRef](#)]
78. Xu, S.; Gao, X.; Hua, Y.; Neville, A.; Wang, Y.; Zhang, K. Rapid deposition of WS<sub>2</sub> platelet thin films as additive-free anode for sodium ion batteries with superior volumetric capacity. *Energy Storage* **2020**, *26*, 534–542. [[CrossRef](#)]
79. Wu, D.; Han, H.; Hong, X.; Tao, S.; Xu, S.; Qian, B.; Wang, L.; Chen, X.; Chu, P.K. A novel self-branching MnCo<sub>2</sub>O<sub>4</sub>/nanographene hybrid composites on macroporous electrically conductive network as bifunctional electrodes for boosting miniature supercapacitors and sodium ion batteries. *J. Alloys Compd.* **2020**, *846*, 155720. [[CrossRef](#)]
80. Li, M.; Wang, Y.; Yang, H.; Chu, P.K. Hierarchical CoMoO<sub>4</sub>@Co<sub>3</sub>O<sub>4</sub> nanocomposites on an ordered macro-porous electrode plate as a multi-dimensional electrode in high-performance supercapacitors. *J. Mater. Chem. A* **2017**, *5*, 17312–17324. [[CrossRef](#)]
81. Wu, D.; Zhang, C.; Liang, C.; Zhu, Y.; Xu, S.; Xiong, D.; Xue, S.; Wang, L.; Chu, P.K. Preparation of multi-layer graphene on nickel-coated silicon microchannel plates by a hydrothermal carbonization procedure and its improved field emission properties. *J. Mater. Chem. C* **2016**, *4*, 2079–2087. [[CrossRef](#)]
82. Chen, C.; Liu, B.; Ru, Q.; Ma, S.; An, B.; Hou, X.; Hu, S. Fabrication of cubic spinel MnCo<sub>2</sub>O<sub>4</sub> nanoparticles embedded in graphene sheets with their improved lithium-ion and sodium-ion storage properties. *J. Power Sources* **2016**, *326*, 252–263. [[CrossRef](#)]
83. Wu, L.; Lang, J.; Zhang, P.; Zhang, X.; Guo, R.; Yan, X. Mesoporous Ni-doped MnCo<sub>2</sub>O<sub>4</sub> hollow nanotubes as an anode material for sodium ion batteries with ultralong life and pseudocapacitive mechanism. *J. Mater. Chem. A* **2016**, *4*, 18392–18400. [[CrossRef](#)]
84. Wang, Y.; Huang, H.; Xie, Q.; Wang, Y.; Qu, B. Rational design of graphene-encapsulated NiCo<sub>2</sub>O<sub>4</sub> core-shell nanostructures as an anode material for sodium-ion batteries. *J. Alloys Compd.* **2017**, *705*, 314–319. [[CrossRef](#)]
85. Saravanakumar, B.; Wang, X.; Zhang, W.; Xing, L.; Li, W. Holey two-dimensional manganese cobalt oxide nanosheets as a high-performance electrode for supercapattery. *Chem. Eng. J.* **2019**, *373*, 547–555. [[CrossRef](#)]
86. Wu, X.; Wu, W.; Wang, K.; Chen, W.; He, D. Synthesis and electrochemical performance of flower-like MnCo<sub>2</sub>O<sub>4</sub> as an anode material for sodium ion batteries. *Mater. Lett.* **2015**, *147*, 85–87. [[CrossRef](#)]
87. Wu, L.; Lang, J.; Wang, R.; Guo, R.; Yan, X. Electrospinning Synthesis of Mesoporous MnCoNiO<sub>x</sub>@Double-Carbon Nanofibers for Sodium-Ion Battery Anodes with Pseudocapacitive Behavior and Long Cycle Life. *ACS Appl. Mater. Inter.* **2016**, *8*, 34342–34352. [[CrossRef](#)]
88. Wu, X.; Wu, W.; Li, Y.; Li, F.; Liao, S. Synthesis and electrochemical performance of rod-like CuFe<sub>2</sub>O<sub>4</sub> as an anode material for Na-ion battery. *Mater. Lett.* **2015**, *138*, 192–195. [[CrossRef](#)]
89. Wang, B.; Li, F.; Wang, X.; Wang, G.; Wang, H.; Bai, J. Mn<sub>3</sub>O<sub>4</sub> nanotubes encapsulated by porous graphene sheets with enhanced electrochemical properties for lithium/sodium-ion batteries. *Chem. Eng. J.* **2019**, *364*, 57–69. [[CrossRef](#)]
90. Jo, M.S.; Lee, J.S.; Jeong, S.Y.; Kim, J.K.; Kang, Y.C.; Kang, D.W.; Jeong, S.M.; Cho, J.S. Golden Bristlegrass-Like Hierarchical Graphene Nanofibers Entangled with N-Doped CNTs Containing CoSe<sub>2</sub> Nanocrystals at Each Node as Anodes for High-Rate Sodium-Ion Batteries. *Small* **2020**, *16*, 2003391. [[CrossRef](#)]

91. Choi, C.H.; Park, S.H.; Woo, S.I. N-doped carbon prepared by pyrolysis of dicyandiamide with various  $\text{MeCl}_2 \cdot x\text{H}_2\text{O}$  (Me=Co, Fe, and Ni) composites: Effect of type and amount of metal seed on oxygen reduction reactions. *Appl. Catal. B* **2012**, *119–120*, 123–131. [[CrossRef](#)]
92. Park, S.-K.; Kang, Y.C. MOF-Templated N-Doped Carbon-Coated  $\text{CoSe}_2$  Nanorods Supported on Porous CNT Microspheres with Excellent Sodium-Ion Storage and Electrocatalytic Properties. *ACS Appl. Mater. Inter.* **2018**, *10*, 17203–17213. [[CrossRef](#)] [[PubMed](#)]
93. Tang, Y.; Zhao, Z.; Hao, X.; Wang, Y.; Liu, Y.; Hou, Y.; Yang, Q.; Wang, X.; Qiu, J. Engineering hollow polyhedrons structured from carbon-coated  $\text{CoSe}_2$  nanospheres bridged by CNTs with boosted sodium storage performance. *J. Mater. Chem. A* **2017**, *5*, 13591–13600. [[CrossRef](#)]
94. Tabassum, H.; Zhi, C.; Hussain, T.; Qiu, T.; Aftab, W.; Zou, R. Encapsulating Trogtalite  $\text{CoSe}_2$  Nanobuds into BCN Nanotubes as High Storage Capacity Sodium Ion Battery Anodes. *Adv. Energy Mater.* **2019**, *9*, 1901778. [[CrossRef](#)]
95. Xu, Y.; Jian, G.; Liu, Y.; Zhu, Y.; Zachariah, M.R.; Wang, C. Superior electrochemical performance and structure evolution of mesoporous  $\text{Fe}_2\text{O}_3$  anodes for lithium-ion batteries. *Nano Energy* **2014**, *3*, 26–35. [[CrossRef](#)]
96. Cho, J.S.; Hong, Y.J.; Kang, Y.C. Design and Synthesis of Bubble-Nanorod-Structured  $\text{Fe}_2\text{O}_3$ -Carbon Nanofibers as Advanced Anode Material for Li-Ion Batteries. *ACS Nano* **2015**, *9*, 4026–4035. [[CrossRef](#)]
97. Park, S.-K.; Lee, J.-K.; Kang, Y.C. Yolk-Shell Structured Assembly of Bamboo-Like Nitrogen-Doped Carbon Nanotubes Embedded with Co Nanocrystals and Their Application as Cathode Material for Li-S Batteries. *Adv. Funct. Mater.* **2018**, *28*, 1705264. [[CrossRef](#)]
98. Cho, J.S.; Won, J.M.; Lee, J.-K.; Kang, Y.C. Design and synthesis of multiroom-structured metal compounds-carbon hybrid microspheres as anode materials for rechargeable batteries. *Nano Energy* **2016**, *26*, 466–478. [[CrossRef](#)]
99. Fang, Y.; Liu, Q.; Feng, X.; Chen, W.; Ai, X.; Wang, L.; Wang, L.; Ma, Z.; Ren, Y.; Yang, H.; et al. An advanced low-cost cathode composed of graphene-coated  $\text{Na}_{2.4}\text{Fe}_{1.8}(\text{SO}_4)_3$  nanograins in a 3D graphene network for ultra-stable sodium storage. *J. Energy Chem.* **2021**, *54*, 564–570. [[CrossRef](#)]
100. Zeng, T.; Feng, D.; Xie, Y.; Jiao, X. Nano  $\text{Sn}_4\text{P}_3$  embedded in nitrogenous carbon matrix as the anode of sodium ion battery for enhanced cyclability. *J. Alloys Compd.* **2021**, *874*, 159944. [[CrossRef](#)]
101. Zhao, W.; Ma, X.; Gao, L.; Li, Y.; Wang, G.; Sun, Q. Engineering carbon-nanochain concatenated hollow  $\text{Sn}_4\text{P}_3$  nanospheres architectures as ultrastable and high-rate anode materials for sodium ion batteries. *Carbon* **2020**, *167*, 736–745. [[CrossRef](#)]
102. Zhu, H.; Jia, Z.; Chen, Y.; Weadock, N.; Wan, J.; Vaaland, O.; Han, X.; Li, T.; Hu, L. Tin Anode for Sodium-Ion Batteries Using Natural Wood Fiber as a Mechanical Buffer and Electrolyte Reservoir. *Nano Lett.* **2013**, *13*, 3093–3100. [[CrossRef](#)] [[PubMed](#)]
103. Mo, R.; Rooney, D.; Sun, K.; Yang, H.Y. 3D nitrogen-doped graphene foam with encapsulated germanium/nitrogen-doped graphene yolk-shell nanoarchitecture for high-performance flexible Li-ion battery. *Nat. Commun.* **2017**, *8*, 13949. [[CrossRef](#)] [[PubMed](#)]
104. Gu, Q.; Kimpton, J.A.; Brand, H.E.A.; Wang, Z.; Chou, S. Solving Key Challenges in Battery Research Using In Situ Synchrotron and Neutron Techniques. *Adv. Energy Mater.* **2017**, *7*, 1602831. [[CrossRef](#)]
105. Xu, Y.; Zhu, Y.; Liu, Y.; Wang, C. Electrochemical Performance of Porous Carbon/Tin Composite Anodes for Sodium-Ion and Lithium-Ion Batteries. *Adv. Energy Mater.* **2013**, *3*, 128–133. [[CrossRef](#)]
106. Ellis, L.D.; Hatchard, T.D.; Obrovac, M.N. Reversible Insertion of Sodium in Tin. *J. Electrochem. Soc.* **2012**, *159*, A1801–A1805. [[CrossRef](#)]
107. Barpanda, P.; Oyama, G.; Nishimura, S.-i.; Chung, S.-C.; Yamada, A. A 3.8-V earth-abundant sodium battery electrode. *Nat. Commun.* **2014**, *5*, 4358. [[CrossRef](#)]
108. Meng, Y.; Yu, T.; Zhang, S.; Deng, C. Top-down synthesis of muscle-inspired alluaudite  $\text{Na}_{2+2x}\text{Fe}_{2-x}(\text{SO}_4)_3$ /SWNT spindle as a high-rate and high-potential cathode for sodium-ion batteries. *J. Mater. Chem. A* **2016**, *4*, 1624–1631. [[CrossRef](#)]
109. Oyama, G.; Pecher, O.; Griffith, K.J.; Nishimura, S.-i.; Pigliapochi, R.; Grey, C.P.; Yamada, A. Sodium Intercalation Mechanism of 3.8 V Class Alluaudite Sodium Iron Sulfate. *Chem. Mater.* **2016**, *28*, 5321–5328. [[CrossRef](#)]
110. Yao, G.; Zhang, X.; Yan, Y.; Zhang, J.; Song, K.; Shi, J.; Mi, L.; Zheng, J.; Feng, X.; Chen, W. Facile synthesis of hierarchical  $\text{Na}_2\text{Fe}(\text{SO}_4)_2$ @rGO/C as high-voltage cathode for energy density-enhanced sodium-ion batteries. *J. Energy Chem.* **2020**, *50*, 387–394. [[CrossRef](#)]
111. Oyama, G.; Nishimura, S.I.; Suzuki, Y.; Okubo, M.; Yamada, A. Off-Stoichiometry in Alluaudite-Type Sodium Iron Sulfate  $\text{Na}_{2+2x}\text{Fe}_{2-x}(\text{SO}_4)_3$  as an Advanced Sodium Battery Cathode Material. *ChemElectroChem* **2015**, *2*, 1019–1023. [[CrossRef](#)]
112. Chen, M.; Cortie, D.; Hu, Z.; Jin, H.; Wang, S.; Gu, Q.; Hua, W.; Wang, E.; Lai, W.; Chen, L.; et al. A Novel Graphene Oxide Wrapped  $\text{Na}_2\text{Fe}_2(\text{SO}_4)_3$ /C Cathode Composite for Long Life and High Energy Density Sodium-Ion Batteries. *Adv. Energy Mater.* **2018**, *8*, 1800944. [[CrossRef](#)]
113. Dwibedi, D.; Ling, C.D.; Araujo, R.B.; Chakraborty, S.; Duraisamy, S.; Munichandraiah, N.; Ahuja, R.; Barpanda, P. Ionothermal Synthesis of High-Voltage Alluaudite  $\text{Na}_{2+2x}\text{Fe}_{2-x}(\text{SO}_4)_3$  Sodium Insertion Compound: Structural, Electronic, and Magnetic Insights. *ACS Appl. Mater. Interfaces* **2016**, *8*, 6982–6991. [[CrossRef](#)] [[PubMed](#)]
114. Fang, Y.; Xiao, L.; Qian, J.; Ai, X.; Yang, H.; Cao, Y. Mesoporous Amorphous  $\text{FePO}_4$  Nanospheres as High-Performance Cathode Material for Sodium-Ion Batteries. *Nano Lett.* **2014**, *14*, 3539–3543. [[CrossRef](#)] [[PubMed](#)]

115. Fang, Y.; Liu, Q.; Xiao, L.; Ai, X.; Yang, H.; Cao, Y. High-Performance Olivine NaFePO<sub>4</sub> Microsphere Cathode Synthesized by Aqueous Electrochemical Displacement Method for Sodium Ion Batteries. *ACS Appl. Mater. Interfaces* **2015**, *7*, 17977–17984. [[CrossRef](#)]
116. Kawabe, Y.; Yabuuchi, N.; Kajiyama, M.; Fukuhara, N.; Inamasu, T.; Okuyama, R.; Nakai, I.; Komaba, S. Synthesis and electrode performance of carbon coated Na<sub>2</sub>FePO<sub>4</sub>F for rechargeable Na batteries. *Electrochem. Commun.* **2011**, *13*, 1225–1228. [[CrossRef](#)]
117. Barpanda, P.; Ye, T.; Nishimura, S.I.; Chung, S.C.; Yamada, Y.; Okubo, M.; Zhou, H.; Yamada, A. Sodium iron pyrophosphate: A novel 3.0V iron-based cathode for sodium-ion batteries. *Electrochem. Commun.* **2012**, *24*, 116–119. [[CrossRef](#)]
118. Liu, M.; Zhang, P.; Qu, Z.; Yan, Y.; Lai, C.; Liu, T.; Zhang, S. Conductive carbon nanofiber interpenetrated graphene architecture for ultra-stable sodium ion battery. *Nat. Commun.* **2019**, *10*, 3917. [[CrossRef](#)]
119. Liu, C.; Zhang, M.; Zhang, X.; Wan, B.; Li, X.; Gou, H.; Wang, Y.; Yin, F.; Wang, G. 2D Sandwiched Nano Heterostructures Endow MoSe<sub>2</sub>/TiO<sub>2-x</sub>/Graphene with High Rate and Durability for Sodium Ion Capacitor and Its Solid Electrolyte Interphase Dependent Sodiation/Desodiation Mechanism. *Small* **2020**, *16*, 2004457. [[CrossRef](#)]
120. Li, M.; Li, S.; Wang, J.; Wang, C.; Li, W.; Chu, P.K. NiFeP nanoflakes composite with CoP on carbon cloth as flexible and durable electrocatalyst for efficient overall water splitting. *Nanotechnology* **2019**, *30*, 485402. [[CrossRef](#)]
121. Minakshi, M.; Barmi, M.; Mitchell, D.R.; Barlow, A.J.; Fichtner, M. Effect of oxidizer in the synthesis of NiO anchored nanostructure nickel molybdate for sodium-ion battery. *Mater. Today Energy* **2018**, *10*, 1–14. [[CrossRef](#)]
122. Minakshi, M.; Mitchell, D.R.; Munnangi, A.R.; Barlow, A.J.; Fichtner, M. New insights into the electrochemistry of magnesium molybdate hierarchical architectures for high performance sodium devices. *Nanoscale* **2018**, *10*, 13277–13288. [[CrossRef](#)]
123. Zhang, X.; Zhao, R.; Wu, Q.; Li, W.; Shen, C.; Ni, L.; Yan, H.; Diao, G.; Chen, M. Petal-like MoS<sub>2</sub> nanosheets space-confined in hollow mesoporous carbon spheres for enhanced lithium storage performance. *ACS Nano* **2017**, *11*, 8429–8436. [[CrossRef](#)] [[PubMed](#)]
124. Shan, T.; Xin, S.; You, Y.; Cong, H.; Manthiram, A. Combining Nitrogen-Doped Graphene Sheets and MoS<sub>2</sub>: A Unique Film–Foam–Film Structure for Enhanced Lithium Storage. *Angew. Chem. Int. Ed.* **2016**, *55*, 12783–12788. [[CrossRef](#)] [[PubMed](#)]
125. Wang, D.; Xing, W.; Lei, S.; Yuan, H. Space-Confined Growth of Defect-Rich Molybdenum Disulfide Nanosheets within Graphene: Application in The Removal of Smoke Particles and Toxic Volatiles. *ACS Appl. Mater. Inter.* **2016**, *8*, 34735. [[CrossRef](#)]
126. Anwer, S.; Huang, Y.; Li, B.; Govindan, B.; Liao, K.; Cantwell, W.J.; Wu, F.; Chen, R.; Zheng, L. Nature-Inspired, Graphene-Wrapped 3D MoS<sub>2</sub> Ultrathin Microflower Architecture as a High-Performance Anode Material for Sodium-Ion Batteries. *ACS Appl. Mater. Inter.* **2019**, *11*, 22323–22331. [[CrossRef](#)] [[PubMed](#)]
127. Chen, C.; Wu, M.; Xu, Z.; Feng, T.; Yang, J.; Chen, Z.; Wang, S.; Wang, Y. Tailored N-doped porous carbon nanocomposites through MOF self-assembling for Li/Na ion batteries. *J. Colloid. Interfaces Sci.* **2019**, *538*, 267–276. [[CrossRef](#)]
128. Desai, A.V.; Morris, R.E.; Armstrong, A.R. Advances in Organic Anode Materials for Na-/K-Ion Rechargeable Batteries. *ChemSusChem* **2020**, *13*, 4866–4884. [[CrossRef](#)] [[PubMed](#)]
129. Deng, J.; Luo, W.-B.; Chou, S.-L.; Liu, H.-K.; Dou, S.-X. Sodium-Ion Batteries: From Academic Research to Practical Commercialization. *Adv. Energy Mater.* **2018**, *8*, 1701428. [[CrossRef](#)]
130. Tang, W.; Liang, R.; Li, D.; Yu, Q.; Hu, J.; Cao, B.; Fan, C. Highly Stable and High Rate-Performance Na-Ion Batteries Using Polyanionic Anthraquinone as the Organic Cathode. *ChemSusChem* **2019**, *12*, 2181–2185. [[CrossRef](#)]
131. Su, Q.; Zeng, S.; Tang, M.; Zheng, Z.; Wang, Z. Flexible Carbon Nanofibrous Membranes with Adjustable Hierarchical Porous Structure as High-Capacity Anodes for Sodium-Ion Batteries. *Energy Technol.* **2021**, *9*, 2100049. [[CrossRef](#)]
132. Wang, L.; Lin, C.; Liang, T.; Wang, N.; Feng, J.; Yan, W. NiSe<sub>2</sub> encapsulated in N-doped TiN/carbon nanoparticles intertwined with CNTs for enhanced Na-ion storage by pseudocapacitance. *Ceram. Int.* **2022**, *48*, 14098–14106. [[CrossRef](#)]
133. Park, S.; Paek, E. Can P-and Oxidized P-doped Graphene be a Good Anode for Na-Ion Batteries? A First-Principles Assessment. *J. Electrochem. Soc.* **2022**, *169*, 050529. [[CrossRef](#)]
134. Zhang, Y.; Xia, X.; Liu, B.; Deng, S.; Xie, D.; Liu, Q.; Wang, Y.; Wu, J.; Wang, X.; Tu, J. Multi-scale graphene-based materials for applications in sodium ion batteries. *Adv. Energy Mater.* **2019**, *9*, 1803342. [[CrossRef](#)]
135. Esfandiari, A.; Haghghat-Shishavan, S.; Nazarian-Samani, M.; Nazarian-Samani, M.; Ramakrishna, S.; Kashani-Bozorg, S.F.; Kim, K.B. Defect-rich Ni<sub>3</sub>Sn<sub>4</sub> quantum dots anchored on graphene sheets exhibiting unexpected reversible conversion reactions with exceptional lithium and sodium storage performance. *Appl. Surf. Sci.* **2020**, *526*, 146756. [[CrossRef](#)]
136. Zhu, Y.; Chen, M.; Li, Q.; Yuan, C.; Wang, C. A porous biomass-derived anode for high-performance sodium-ion batteries. *Carbon* **2018**, *129*, 695–701. [[CrossRef](#)]
137. Wang, P.; Zhu, K.; Ye, K.; Gong, Z.; Liu, R.; Cheng, K.; Cao, D. Three-dimensional bio-mass derived hard carbon with reconstructed surface as a free-standing anode for sodium-ion batteries. *J. Colloid Interf. Sci.* **2020**, *561*, 203–210. [[CrossRef](#)]
138. Wang, Z.; Liu, B.; Xie, J.; Hu, J.; Lu, Z.; Cao, Y. Phosphorus/sulfur co-doped hard carbon with a well-designed porous bowl-like structure and enhanced initial coulombic efficiency for high-performance sodium storage. *J. Alloys Compd.* **2022**, *911*, 164979. [[CrossRef](#)]

139. Thakur, A.K.; Ahmed, M.S.; Oh, G.; Kang, H.; Jeong, Y.; Prabakaran, R.; Vikram, M.P.; Sharshir, S.W.; Kim, J.; Hwang, J.Y. Advancement in graphene-based nanocomposites as high capacity anode materials for sodium-ion batteries. *J. Mater. Chem. A* **2021**, *9*, 2628–2661. [[CrossRef](#)]
140. Su, D.; Wang, C.; Ahn, H.J.; Wang, G. Single crystalline  $\text{Na}_{0.7}\text{MnO}_2$  nanoplates as cathode materials for sodium-ion batteries with enhanced performance. *Chem.–Eur. J.* **2013**, *19*, 10884–10889. [[CrossRef](#)]
141. Vassilaras, P.; Ma, X.; Li, X.; Ceder, G. Electrochemical properties of monoclinic  $\text{NaNiO}_2$ . *J. Electrochem. Soc.* **2012**, *160*, A207. [[CrossRef](#)]
142. Ding, J.J.; Zhou, Y.N.; Sun, Q.; Yu, X.Q.; Yang, X.Q.; Fu, Z.W. Electrochemical properties of P2-phase  $\text{Na}_{0.74}\text{CoO}_2$  compounds as cathode material for rechargeable sodium-ion batteries. *Electrochim. Acta* **2013**, *87*, 388–393. [[CrossRef](#)]
143. Raju, V.; Rains, J.; Gates, C.; Luo, W.; Wang, X.; Stickle, W.F.; Stucky, G.D.; Ji, X. Superior cathode of sodium-ion batteries: Orthorhombic  $\text{V}_2\text{O}_5$  nanoparticles generated in nanoporous carbon by ambient hydrolysis deposition. *Nano Lett.* **2014**, *14*, 4119–4124. [[CrossRef](#)] [[PubMed](#)]
144. Wei, Q.; Liu, J.; Feng, W.; Sheng, J.; Tian, X.; He, L.; An, Q.; Mai, L. Hydrated vanadium pentoxide with superior sodium storage capacity. *J. Mater. Chem. A* **2015**, *3*, 8070–8075. [[CrossRef](#)]
145. Li, Y.; Wang, D.; An, Q.; Ren, B.; Rong, Y.; Yao, Y. Flexible electrode for long-life rechargeable sodium-ion batteries: Effect of oxygen vacancy in  $\text{MoO}_{3-x}$ . *J. Mater. Chem. A* **2016**, *4*, 5402–5405. [[CrossRef](#)]
146. Li, S.; Dong, Y.; Xu, L.; Xu, X.; He, L.; Mai, L. Effect of carbon matrix dimensions on the electrochemical properties of  $\text{Na}_3\text{V}_2(\text{PO}_4)_3$  nanograins for high-performance symmetric sodium-ion batteries. *Adv. Mater.* **2014**, *26*, 3545–3553. [[CrossRef](#)]
147. Zhu, C.; Song, K.; van Aken, P.A.; Maier, J.; Yu, Y. Carbon-coated  $\text{Na}_3\text{V}_2(\text{PO}_4)_3$  embedded in porous carbon matrix: An ultrafast Na-storage cathode with the potential of outperforming Li cathodes. *Nano Lett.* **2014**, *14*, 2175–2180. [[CrossRef](#)]
148. Kim, H.; Shakoor, R.A.; Park, C.; Lim, S.Y.; Kim, J.S.; Jo, Y.N.; Cho, W.; Miyasaka, K.; Kahraman, R.; Jung, Y.; et al.  $\text{Na}_2\text{FeP}_2\text{O}_7$  as a promising iron-based pyrophosphate cathode for sodium rechargeable batteries: A combined experimental and theoretical study. *Adv. Funct. Mat.* **2013**, *23*, 1147–1155. [[CrossRef](#)]
149. Barpanda, P.; Ye, T.; Avdeev, M.; Chung, S.C.; Yamada, A. A new polymorph of  $\text{Na}_2\text{MnP}_2\text{O}_7$  as a 3.6 V cathode material for sodium-ion batteries. *J. Mater. Chem. A* **2013**, *1*, 4194–4197. [[CrossRef](#)]
150. Barpanda, P.; Lu, J.; Ye, T.; Kajiyama, M.; Chung, S.C.; Yabuuchi, N.; Komaba, S.; Yamada, A. A layer-structured  $\text{Na}_2\text{CoP}_2\text{O}_7$  pyrophosphate cathode for sodium-ion batteries. *Rsc Adv.* **2013**, *3*, 3857–3860. [[CrossRef](#)]
151. Singh, P.; Shiva, K.; Celio, H.; Goodenough, J.B. Eldferrite,  $\text{NaFe}(\text{SO}_4)_2$ : An intercalation cathode host for low-cost Na-ion batteries. *Energy Environ. Sci.* **2015**, *8*, 3000–3005. [[CrossRef](#)]
152. Sarwar, M.K.; Xu, Z.; Yao, K.; Liu, X.; Wang, Y.; Yang, J.; Huang, J. Constructing N-Doped graphene supported  $\text{MoS}_2@ \text{Ni}_3\text{S}_4$  for pseudocapacitive sodium-ion storage with high rate and long life. *Mater. Today Chem.* **2022**, *23*, 100713.
153. Aristote, N.T.; Zou, K.; Di, A.; Deng, W.; Wang, B.; Deng, X.; Hou, S.; Zou, G.; Ji, X. Methods of improving the initial Coulombic efficiency and rate performance of both anode and cathode materials for sodium-ion batteries. *Chin. Chem. Lett.* **2021**, *33*, 730–742. [[CrossRef](#)]
154. Tang, Z.; Zhou, S.; Wu, P.; Wang, H.; Huang, Y.; Zhang, Y.; Sun, D.; Tang, T.; Wang, H. Engineering surface oxygenated functionalities on commercial hard carbon toward superior sodium storage. *Chem. Eng. J.* **2022**, *441*, 135899. [[CrossRef](#)]
155. Beheshti, S.H.; Javanbakht, M.; Omidvar, H.; Hosen, M.S.; Hubin, A.; Van Mierlo, J.; Bercibar, M. Development, Retainment and Assessment of the Graphite-Electrolyte Interphase in Li-ion Batteries Regarding the Functionality of SEI-Forming Additives. *Iscience* **2022**, *25*, 103862. [[CrossRef](#)]
156. Fang, Y.; Xiao, L.; Qian, J.; Cao, Y.; Ai, X.; Huang, Y.; Yang, H. 3D graphene decorated  $\text{NaTi}_2(\text{PO}_4)_3$  microspheres as a superior high-rate and ultracycle-stable anode material for sodium ion batteries. *Adv. Energy Mater.* **2016**, *6*, 1502197. [[CrossRef](#)]
157. Kim, H.; Kim, H.; Kim, H.; Kim, J.; Yoon, G.; Lim, K.; Yoon, W.-S.; Kang, K. Understanding origin of voltage hysteresis in conversion reaction for Na rechargeable batteries: The case of cobalt oxides. *Adv. Funct. Mater.* **2016**, *26*, 5042–5050. [[CrossRef](#)]
158. Peng, S.; Han, X.; Li, L.; Zhu, Z.; Cheng, F.; Srinivansan, M.; Adams, S.; Ramakrishna, S. Unique cobalt sulfide/reduced graphene oxide composite as an anode for sodium-ion batteries with superior rate capability and long cycling stability. *Small* **2016**, *12*, 1359–1368. [[CrossRef](#)]
159. Teng, Y.; Zhao, H.; Zhang, Z.; Zhao, L.; Zhang, Y.; Li, Z.; Xia, Q.; Du, Z.; Świerczek, K.  $\text{MoS}_2$  nanosheets vertically grown on reduced graphene oxide via oxygen bonds with carbon coating as ultrafast sodium ion batteries anodes. *Carbon* **2017**, *119*, 91–100. [[CrossRef](#)]
160. Qu, B.; Ma, C.; Ji, G.; Xu, C.; Xu, J.; Meng, Y.S.; Wang, T.; Lee, J.Y. Layered  $\text{SnS}_2$ -reduced graphene oxide composite—A high-capacity, high-rate, and long-cycle life sodium-ion battery anode material. *Adv. Mater.* **2014**, *26*, 3854–3859. [[CrossRef](#)]
161. Xiong, X.; Wang, G.; Lin, Y.; Wang, Y.; Ou, X.; Zheng, F.; Yang, C.; Wang, J.-H.; Liu, M. Enhancing sodium ion battery performance by strongly binding nanostructured  $\text{Sb}_2\text{S}_3$  on sulfur-doped graphene sheets. *ACS Nano* **2016**, *10*, 10953–10959. [[CrossRef](#)] [[PubMed](#)]
162. Xu, Y.; Peng, B.; Mulder, F.M. A high-rate and ultrastable sodium ion anode based on a novel  $\text{Sn}_4\text{P}_3\text{-P@graphene}$  nanocomposite. *Adv. Energy Mater.* **2018**, *8*, 1701847. [[CrossRef](#)]

163. Xiong, X.; Yang, C.; Wang, G.; Lin, Y.; Ou, X.; Wang, J.H.; Zhao, B.; Liu, M.; Lin, Z.; Huang, K. SnS nanoparticles electrostatically anchored on three-dimensional N-doped graphene as an active and durable anode for sodium-ion batteries. *Energy Environ. Sci.* **2017**, *10*, 1757–1763. [[CrossRef](#)]
164. Lu, Y.; Zhang, N.; Jiang, S.; Zhang, Y.; Zhou, M.; Tao, Z.; Archer, L.A.; Chen, J. High-capacity and ultrafast Na-ion storage of a self-supported 3D porous antimony persulfide–graphene foam architecture. *Nano Lett.* **2017**, *17*, 3668–3674. [[CrossRef](#)] [[PubMed](#)]
165. Zhang, J.; Fang, Y.; Xiao, L.; Qian, J.; Cao, Y.; Ai, X.; Yang, H. Graphene-scaffolded Na<sub>3</sub>V<sub>2</sub>(PO<sub>4</sub>)<sub>3</sub> microsphere cathode with high rate capability and cycling stability for sodium ion batteries. *ACS Appl. Mater. Interfaces* **2017**, *9*, 7177–7184. [[CrossRef](#)]
166. Li, H.; Chen, X.; Jin, T.; Bao, W.; Zhang, Z.; Jiao, L. Robust graphene layer modified Na<sub>2</sub>Mn<sub>2</sub>P<sub>2</sub>O<sub>7</sub> as a durable high-rate and high energy cathode for Na-ion batteries. *Energy Storage Mater.* **2019**, *16*, 383–390. [[CrossRef](#)]